

13 **Abstract**

14 Ocean Island Basalts (OIBs) are generated by mantle plumes, with their geochem-
 15 istry controlled by a combination of source composition, temperature, and thickness of
 16 overlying lithosphere. For example, OIBs erupting onto thicker, older oceanic lithosphere
 17 are expected to exhibit signatures indicative of higher average melting pressures. Here,
 18 we quantitatively investigate this relationship using a global dataset of Neogene and younger
 19 OIB compositions. Local lithospheric thicknesses are estimated using theoretical plate-
 20 cooling models and Bayes factors are applied to identify trends. Our findings provide com-
 21 pelling evidence for a correlation between OIB geochemistry and lithospheric thickness,
 22 with some variables (SiO_2 , Al_2O_3 , FeO , Lu, Yb and λ_2) showing linear trends that can
 23 be attributed to increasing average melting pressure, whereas others (λ_0 and λ_1 , CaO)
 24 require a bi-linear fit with a change in gradient at ~ 55 km. Observed variations in highly
 25 incompatible elements are consistent with melt fractions that decrease with increasing
 26 lithospheric thickness, as expected. Nevertheless, at thicknesses beyond ~ 55 km, the
 27 implied melt fraction does not decrease as rapidly as suggested by theoretical expecta-
 28 tions. This observation is robust across different lithospheric thickness estimates, includ-
 29 ing those derived from seismic constraints. We interpret this result as weak plumes fail-
 30 ing to effectively thin overlying lithosphere and/or producing insufficient melt to erupt
 31 at the surface, in combination with a ‘memory effect’ of incomplete homogenisation of
 32 melts during their ascent. This view is supported by independent estimates of plume buoy-
 33 ancy flux, indicating that OIB magmatism on older lithosphere may be biased towards
 34 hotter plumes.

35 **Plain Language Summary**

36 Most of Earth’s volcanoes occur at tectonic plate boundaries, but some emerge within
 37 plate interiors in so-called intra-plate settings. These volcanoes are believed to mark the
 38 surface expression of mantle plumes: hot, buoyant columns that rise from the core-mantle-
 39 boundary towards the surface. As they rise, lower pressures near the surface facilitate
 40 melting. However, the lithosphere – Earth’s rigid outermost shell – limits plume ascent,
 41 and therefore controls the final (lowest) melting pressure of mantle plumes (the ‘lid ef-
 42 fect’). Here, we collate and analyse a global geochemical dataset of oceanic island basalts
 43 – the products of plume melting – to test this hypothesis. Using a range of diagnostics
 44 and a novel probabilistic analytical approach, we find that some geochemical paramet-
 45 ers either linearly increase or decrease with lithospheric thickness, whereas other trends
 46 exhibit abrupt changes. We propose potential explanations for these patterns, focusing
 47 on factors such as the degree of melting (which is sensitive to temperature and pressure)
 48 and variations in mantle mineralogy at different depths. Notably, we suggest that there
 49 is a higher chance of observing volcanism above hotter plumes in regions of thicker litho-
 50 sphere and identify a ‘memory effect’, whereby their geochemistry preserves information
 51 from the initial melting process.

52 **1 Introduction**

53 While the majority of Earth’s volcanism is concentrated at tectonic plate bound-
 54 aries, there are many volcanic activities that occur within plate interiors and/or extend
 55 across plate boundaries. This volcanism is often associated with mantle plumes – hot,
 56 buoyant columns that rise from the core-mantle boundary towards the surface (e.g., Mor-
 57 gan, 1971; Griffiths & Campbell, 1990, 1991; Duncan & Richards, 1991; Campbell, 2007;
 58 D. R. Davies & Davies, 2009, Figure 1). As they rise into the shallow mantle, plumes
 59 undergo partial melting, with voluminous plume heads giving rise to Large Igneous Provinces
 60 and their tails producing lower fraction melts, termed *Ocean Island Basalts* (OIBs) in
 61 oceanic settings (e.g. White & McKenzie, 1989). The geological, geophysical and geo-
 62 chemical characteristics of OIBs have been widely studied (e.g., White & McKenzie, 1989;

Weaver, 1991; Courtillot et al., 1999; Li et al., 2014; D. R. Davies, Goes, & Sambridge, 2015; Jones et al., 2016; Iaffaldano et al., 2018; Ball et al., 2019; Nebel et al., 2019; Jones et al., 2019; Bao et al., 2022). Nevertheless, despite mantle-plume theory being well established, our understanding remains incomplete concerning the interaction between plumes and overlying lithosphere – Earth’s rigid outermost shell – and its reflection in the geochemistry of OIBs.

The lithospheric mantle is cool and refractory. Accordingly, it is unlikely to melt and generate magmas (e.g., Katz et al., 2003). In addition, the lithosphere is highly viscous and is therefore difficult to mechanically deform (e.g., Burov et al., 2007; Campbell, 2007; Burov & Gerya, 2014; Jones et al., 2017; Duvernay et al., 2021, 2022). As a consequence, it is expected to act as a lid that limits plume ascent and thereby dictate the lowest melting pressure for plume-derived melts (Figure 1). This behaviour is the so-called ‘*lid effect*’, first proposed by Watson and McKenzie (1991) and subsequently examined in several studies at both global (e.g. Ellam, 1992; Humphreys & Niu, 2009; Dasgupta et al., 2010; Niu et al., 2011; Niu, 2021) and regional scales (e.g. Gibson & Geist, 2010; D. R. Davies, Rawlinson, et al., 2015; Hole & Millett, 2016; Liu et al., 2016; Klöcking et al., 2018). Despite this extensive body of work, a complete and statistically rigorous assessment of the relationship between lithospheric thickness and the geochemistry of plume-derived magmas has not yet been established: previous studies have either described this relationship qualitatively or only made use of simple linear statistics (e.g. Ellam, 1992; Humphreys & Niu, 2009; Niu et al., 2011; D. R. Davies, Rawlinson, et al., 2015; Niu, 2021). Several important questions remain, including:

1. Do available geochemical data statistically support existence of a lid effect?
2. Are observed trends consistent with theoretical expectations for partial melting at different pressures?
3. What other processes might be affecting observed trends?

The last few years have seen progress in several areas that are pertinent to answering these questions. There has been a steady increase in the quantity and accessibility of high-quality data available on melt geochemistry, improvements in the accuracy and resolution of lithospheric thickness datasets, and the advent of robust statistical techniques to examine any potential relationship between the two. There is, therefore, an opportunity to undertake a critical reevaluation of evidence for the lid effect.

Our study exploits an extensive and carefully curated dataset of geochemical analyses for OIBs, extracted from the ever-growing open-source **GeoRoc** database (<https://georoc.eu>). The dataset is filtered to eliminate those samples whose geochemistry has been strongly altered after initial magma generation. Alongside the geochemical parameters examined by previous studies, we analyse geochemical diagnostics on Rare Earth Elements (REEs) that have been recently proposed by O’Neill (2016) and are expected to show a clear pressure signal owing to their sensitivity to melt fraction and the spinel-garnet phase transition. The latter, a pressure-sensitive aluminium-rich phase change, induces a substantial change to the peridotite mineral assemblage, with different REEs exhibiting varying compatibility between the two phases (e.g., Sun & Liang, 2013; Wood et al., 2013). Furthermore, we exploit new estimates of lithospheric thickness, based upon both theoretical models of oceanic spreading and observational constraints from seismic data (Richards, Hoggard, Crosby, et al., 2020; Hoggard, Czarnota, et al., 2020). Using a probabilistic Bayesian approach that is capable of detecting sharp changes in geochemical trends, we investigate the role of lithospheric thickness in controlling OIB geochemistry and explore the mechanisms that underpin the trends that we observe.

The remainder of our paper is structured as follows. In Section 2.1, we introduce our OIB database, our approach to filtering this data, and the geochemical diagnostics examined. In Section 2.2, we describe the lithospheric thickness estimates at each indi-

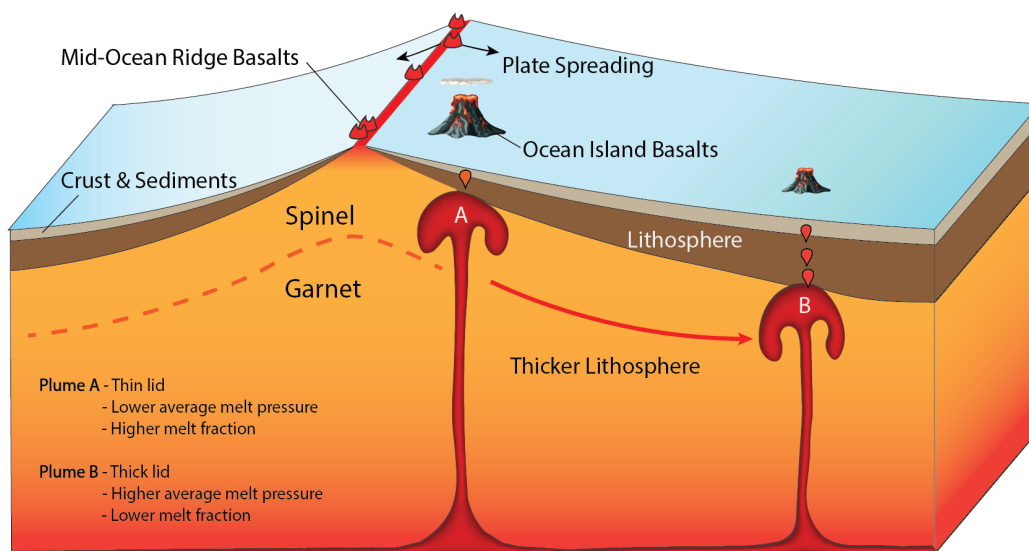


Figure 1. Schematic cartoon illustrating how oceanic lithosphere acts as a lid, hindering the ascent of mantle plumes. When a plume rises beneath thin lithosphere, large melt volumes will be produced with more melts generated within the spinel stability field, thus exhibiting a low-pressure signature. Conversely, when a plume rises beneath thick lithosphere, melt volumes are smaller and melting will principally occur within the garnet stability field, displaying a high-pressure signature.

114 vidual island, derived using both plate-cooling models and local constraints from surface-
 115 wave tomography models. In Section 2.3 we present a probabilistic Bayesian approach
 116 developed and utilised to analyse relationships between geochemistry and lithospheric
 117 thickness. Our results are presented in Section 3, with their sensitivities, implications
 118 for our understanding of the lid-effect, the role of the lithosphere in modulating plume
 119 melting, and other processes affecting OIB chemistry, discussed in Section 4.

120 2 Methods

121 2.1 Geochemical Dataset

122 In compiling our geochemical database of the products of plume melting in oceanic
 123 settings, we have chosen to focus solely on OIB data and neglect data associated with
 124 Large Igneous Provinces (LIPs). This omission is due to the fact that LIPs are the melt-
 125 products of plume heads and are also often associated with continental break-up. They
 126 regularly occur in the vicinity of the continent-ocean boundary and consequently often
 127 display a strong crustal signature (e.g., Chung & Jahn, 1995; Owen-Smith et al., 2017;
 128 J. H. F. L. Davies et al., 2021). It is also therefore difficult to estimate lithospheric thick-
 129 ness at the time of their eruption (e.g., Hill, 1991; Courtillot et al., 1999).

130 2.1.1 Source of Analyses

131 Geochemical data for major and trace element concentrations are compiled from
 132 the GeoRoc database. As the number of high-quality glass samples is limited, the data
 133 are derived principally from analyses of bulk rocks (with some additional glass analy-
 134 ses where available). The GeoRoc database contains geochemical information from over
 135 20,000 OIB samples from the Atlantic, Indian and Pacific Oceans, with their locations

mapped in Figure 2 and listed in Tables S1 and S2. Our database incorporates concentrations of major (SiO_2 , Al_2O_3 , MgO , FeO , TiO_2 , Na_2O , K_2O , CaO , P_2O_5) and trace elements (REEs, U, Nb, Ba, Th), as well as derivative parameters describing REE patterns (λ_0 , λ_1 and λ_2 , from O'Neill, 2016). Major elements with high concentrations are likely influenced by the stabilities of minerals under varying pressure and their compatibilities in mantle peridotite. We expect that major elements with lower concentrations (usually < 5 wt. %) and trace elements are sensitive to phase changes and the degree of melting, which, in turn, are sensitive to pressure. The combined use of both major and trace element parameters can therefore offer a more complete picture of the impact of the lithospheric lid on mantle melting processes.

2.1.2 Database Filtering

Melts generated from peridotite melting are subject to various physiochemical processes during their ascent and whilst residing in magma chambers, such as fractional crystallisation and crustal assimilation (e.g., Sisson & Grove, 1993; Class & Goldstein, 1997; Straub et al., 2013; Ubide et al., 2022). Additionally, post-eruptive hydrothermal alteration can substantially alter the original chemical signature of basalts (e.g., Saito et al., 2015; Khogenkumar et al., 2016). Some previous studies of the lid effect have chosen to use all available OIB geochemical data without attempting to screen samples that are heavily impacted by these additional processes (e.g., Humphreys & Niu, 2009). In our analyses, however, we believe that it is desirable to initially filter OIB samples to isolate those that exhibit a composition most similar to that of the primitive magma. We therefore restrict our dataset to samples that have experienced limited compositional change after magma generation. We do so by applying the following filters to the data:

1. Only those samples with SiO_2 43–54 wt.% are accepted in order to exclude melts that fall outside of the basalt field (Figure 3a);
2. Only samples with MgO 7–16 wt.% are accepted. Values with $\text{MgO} < 7$ wt.% are likely to have been subjected to extensive fractional crystallisation (e.g., Sisson & Grove, 1993) and may contain clinopyroxene and/or plagioclase phenocrysts or have experienced clinopyroxene and plagioclase crystallisation, complicating interpretation of major element trends. Samples with $\text{MgO} > 16$ wt.% are rejected as they are likely to contain olivine phenocrysts (Figures 3a and 3b, e.g., Albarède et al., 1997);
3. Samples with loss on ignition (LOI) > 3 wt.% are rejected to eliminate basalts subjected to excessive levels of post-eruptive hydrothermal alteration (e.g., Greenberger et al., 2012);
4. Samples with $\text{Nb/U} < 30$, $\text{La/Nb} > 1.2$, or La/Ba and Nb/U values outside of the ellipse of Fitton et al. (1991) are all rejected as they are likely to have been contaminated by continental crust (e.g., Rudnick, 1995; Condie, 1999; Hofmann, 2003, Figures 3c and 3d).

Application of these filters to the global OIB dataset results in a subset of 1,737 samples, each consisting of concentrations of major elements, trace elements and REEs.

2.1.3 Correction for Fractional Crystallisation

When magma travels through the lithosphere or remains in a magma chamber, any fractional crystallisation that occurs alters the concentration of major and trace elements in the remaining melt (e.g., M. G. Jackson et al., 2012; Ubide et al., 2022). Provided that the mineral phases that have crystallised are not complex, we can ‘revert’ this process to estimate concentrations of both major and trace elements in the primary magma. To do so, we use the Petrolog3 software (Danyushevsky & Plechov, 2011) to reintroduce olivine into evolved OIBs until MgO concentrations reach 16 wt.%, which is the assumed MgO

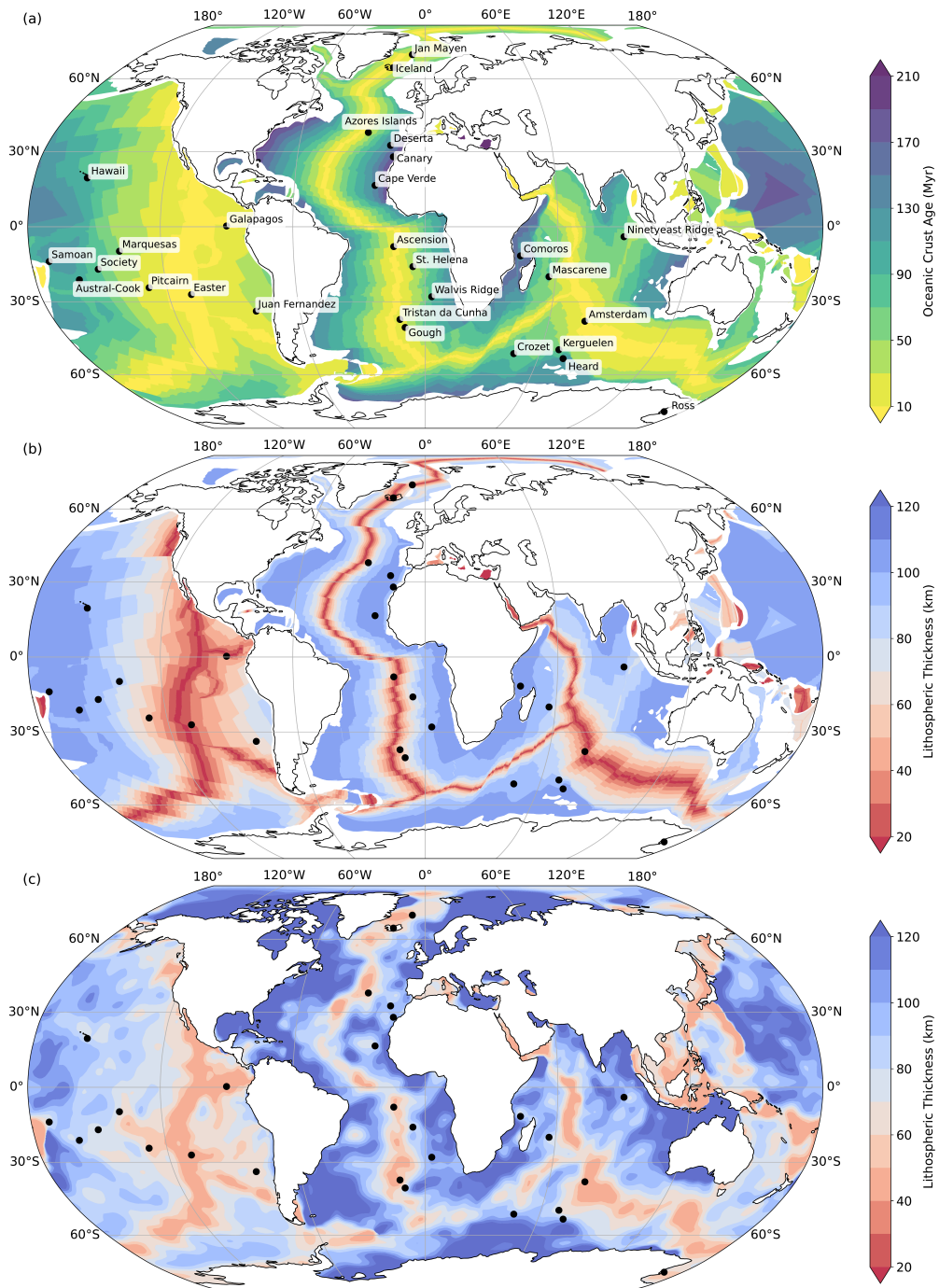


Figure 2. (a) Present-day oceanic lithospheric age from Seton et al. (2020) with locations of selected OIB samples (black dots). Only the name of the archipelago for each island group is displayed, but each individual island's lithospheric age and thickness are considered separately during the analysis. (b) Present-day oceanic lithospheric thickness based on a global plate-cooling model (Richards, Hoggard, Crosby, et al., 2020). (c) Present-day oceanic lithospheric thickness constrained by surface-wave tomography (Hoggard, Czarnota, et al., 2020).

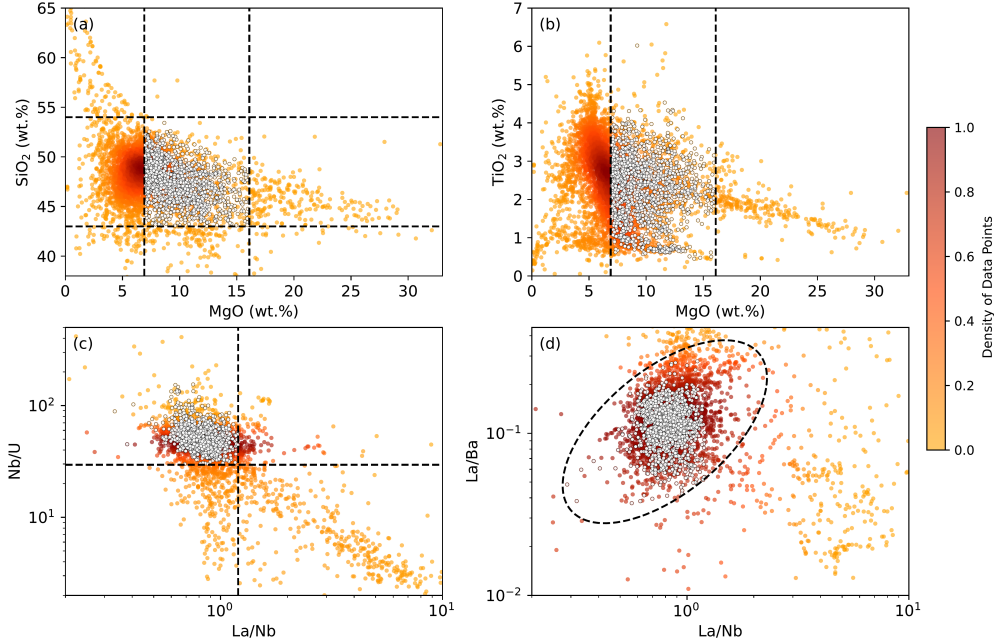


Figure 3. OIB database and sample filtering criteria. (a) SiO₂ versus MgO; coloured dots = original samples coloured by Gaussian kernel density estimation, normalised from 0 to 1; dashed lines = filtering criteria corresponding to SiO₂ 43–54 wt.% and MgO 7–16 wt.%; white circles = subset of data that pass all filtering criteria. (b) Same for TiO₂ versus MgO. (c) Same for Nb/U versus La/Nb, where criteria of > 30 and < 1.2, respectively, are applied. (d) Same for La/Ba versus La/Nb, where only samples inside the ellipse of Fitton et al. (1991) are accepted.

185 content of magma that is in equilibrium with the mantle (e.g., Norman & Garcia, 1999).
 186 Despite some studies showing that minerals fractionate throughout magma ascent (e.g.,
 187 Lundstrom et al., 2003; Liu et al., 2016), we make the simplifying assumption that this
 188 olivine did not crystallise until melts reached a magma chamber at ~ 0.3 GPa (~ 9 km
 189 depth). This choice of depth roughly coincides with the Moho, where the drop in den-
 190 sity from mantle to crustal rocks results in melts becoming neutrally buoyant, allowing
 191 magma to remain in the chamber for a more extended period of time (Ryan, 1988, 1994).
 192 In the continuous, pure fractional crystallisation process, we assume that partition co-
 193 efficients for trace elements in olivine remain constant. For each individual OIB sample,
 194 we use the major element calculations of Petrolog3 to determine how much olivine to ‘add
 195 back in’ to obtain the composition of the primitive magma. Accordingly, the concentra-
 196 tion of each trace element in the primitive magma (c_p) is calculated via

$$197 \quad c_p = \frac{c_1}{(1 - X)^{D-1}}, \quad (1)$$

198 where c_1 is the measured concentration of each element in the sample, X is the fraction
 199 of olivine crystallised, and D is the associated partition coefficient (Shaw, 1970).

200 *2.1.4 Shape of REE patterns*

201 Due to their high charge and large ionic radii, REEs behave as incompatible ele-
 202 ments in most mantle minerals. Moreover, the consistency of REE chemical valence makes
 203 their ionic radius systematically decrease with increasing atomic number (so-called lan-
 204 thanide contraction; Ahrens, 1952). Since REEs occupy identical crystal lattice positions,

205 their partition coefficients therefore exhibit a systematic dependence on atomic number,
 206 with lower atomic number REEs (Light Rare Earth Elements; LREEs) possessing larger
 207 radii and being more incompatible. Accordingly, during partial melting, REEs with a
 208 smaller atomic number more preferentially enter the melt than their heavier counterparts,
 209 an imbalance that is particularly pronounced at low degrees of melting. A caveat to this
 210 basic behaviour is that heavy rare earth elements (HREEs) readily substitute for Al^{3+}
 211 in garnet and, hence, can be compatible in garnet. As such, low-fraction melts gener-
 212 ated within the garnet stability field will have lower HREE concentrations than equiv-
 213 alent melts generated in the spinel stability field. Many laboratory experiments have been
 214 conducted to constrain the partition coefficients of REEs, with results consistent with
 215 these aforementioned theoretical predictions (e.g., Fujimaki et al., 1984; McKenzie & O’Nions,
 216 1991; Johnson, 1994, 1998). It is also worth noting that, due to the general incompat-
 217 ibility of REEs in all low-pressure mineral phases, their relative proportions are gener-
 218 ally unaffected by fractional crystallisation at low pressure.

219 The systematic variation in REE behavior is best illustrated by plotting the log
 220 of their relative abundances as a function of atomic size: as demonstrated by O’Neill (2016),
 221 such patterns can be fit by polynomials with different shape coefficients. Given current
 222 analytical precision, third-order polynomials are usually sufficient to fit measured REE
 223 patterns. Their coefficients are denoted as λ_i (where $i = 0, 1, 2$) and can vary indepen-
 224 dently of one another. λ_i values also have a physical significance: (i) λ_0 measures the
 225 average log concentration of REEs (excluding Eu) normalized to their chondritic con-
 226 centrations, with higher λ_0 indicating higher average REE concentrations; (ii) λ_1 mea-
 227 sures the linear slope of the pattern (with increasing values for larger slopes), where pos-
 228 itive λ_1 values indicate LREE enrichment relative to HREE and negative λ_1 values in-
 229 dicate HREE enrichment relative to LREE; (iii) λ_2 describes the quadratic curvature of
 230 the pattern (with increasing values for larger curvatures), where a concave pattern (pos-
 231 itive λ_2) indicates that amphibole and/or clinopyroxene remains in the residue follow-
 232 ing partial melting and a convex pattern (negative λ_2) indicating that garnet remains
 233 in the residue. In contrast to the simple ratios between two REEs, such as Ce/Y and La/Sm,
 234 that have been extensively used in previous studies (e.g., Ellam, 1992; Humphreys & Niu,
 235 2009; Niu, 2021), λ_i considers all REEs except Eu and is more robust to the idiosyncrasies
 236 of individual element behavior.

237 2.2 Lithospheric Thickness and Eruptive Age

238 The thickness of oceanic lithosphere as a function of ocean floor age is commonly
 239 approximated through one of two theoretical cooling models: (i) the half-space model,
 240 in which lithospheric thickness is proportional to the square root of lithospheric age (Turcotte
 241 & Oxburgh, 1967); and (ii) the plate model, where lithospheric thickness increases with
 242 plate age, but asymptotes towards a constant value beyond a certain age due to heat re-
 243 supply from below (McKenzie, 1967). Plate-model predictions have been shown to pro-
 244 vide an improved match to heat flow and bathymetry observations in older ocean floor
 245 and also inferences of lithosphere-asthenosphere boundary (LAB) depth obtained from
 246 seismology (McKenzie, 1967; Parsons & Sclater, 1977; Richards et al., 2018; Richards,
 247 Hoggard, Crosby, et al., 2020). Accordingly, the plate model is our preferred reference
 248 and we test two different versions of it: one derived from globally averaged subsidence
 249 and heatflow data and the second providing optimal fits to subsets of these data from
 250 each individual oceanic basin (Atlantic, Indian and Pacific Oceans; Richards, Hoggard,
 251 Crosby, et al., 2020). We present results for the latter in the main text and also conduct
 252 assessments of the sensitivity of our results to this choice, with a summary presented in
 253 the Supplementary Information. In all cases, the potential temperature in the model is
 254 fixed to 1333°C and the base of the lithosphere is assumed to follow the $1175 \pm 50^\circ\text{C}$
 255 isotherm.

256 A limitation of theoretical cooling models is that they assume oceanic lithospheric
 257 thickness varies solely as a function of ocean-floor age and, hence, cannot capture local
 258 deviations away from this average behaviour. Seismological observations, particularly
 259 from surface-wave tomography, provide a way of mapping these local variations in litho-
 260 spheric thickness, including those potentially induced by the impingement of mantle plumes
 261 (Ballmer et al., 2011; Schaeffer & Lebedev, 2013; Richards, Hoggard, White, & Ghelichkhan,
 262 2020; Duvernay et al., 2022). Accordingly, to complement our plate-model derived es-
 263 timates of lithospheric thickness and explore the sensitivity of our results to regional litho-
 264 spheric thickness variations, we also make use of a seismologically derived model of litho-
 265 spheric thickness from Hoggard, Czarnota, et al. (2020).

266 We separate ocean islands into two categories: products from off-axis and on-axis
 267 plumes. For off-axis islands, we estimate lithospheric thickness using the aforementioned
 268 plate-cooling and seismologically derived models. Unfortunately, neither theoretical cool-
 269 ing models nor global-scale seismic estimates are good at constraining lithospheric thick-
 270 ness above on-axis plumes. The former do not capture the consequences of increased melt
 271 generation and hence thicker crust above plumes, while the latter suffer from the lim-
 272 ited resolution of surface waves at depths shallower than ~ 75 km (White & McKen-
 273 zie, 1989; Priestley & McKenzie, 2006). For on-axis islands, we therefore obtain litho-
 274 spheric thickness from local estimates of crustal thickness, assuming that melting extended
 275 to the top of the underlying mantle as is observed in ophiolites (e.g., Pallister & Hop-
 276 son, 1981). Seismic estimates for Moho depths are as follows: Iceland ~ 20 – 30 km (White
 277 et al., 1996); Ninetyeast Ridge, ~ 15 – 25 km (Grevemeyer et al., 2001); Walvis Ridge \sim
 278 10 – 25 km (for lithosphere that is now aged between 60 Ma and 100 Ma; Goslin & Sibuet,
 279 1975; Graça et al., 2019). At each of these sites, we calculate average lithospheric thick-
 280 ness according to $\frac{1}{2}(h_{\max}+h_{\min})$, where h_{\max} and h_{\min} are the maximum and minimum
 281 estimates of Moho depth, respectively.

282 Estimating lithospheric thickness at the time of eruption requires knowledge of litho-
 283 spheric age at that time, which can be obtained by subtracting the OIB age from the
 284 present-day lithospheric age (Figure 2a). Present-day lithospheric age for each island is
 285 obtained from the global grid of Seton et al. (2020), with the age range of OIBs on each
 286 island constrained, where possible, by the onset and termination of the shield stage of
 287 volcanism or, in cases where geological constraints on the shield period are unavailable
 288 or unclear, the maximum and minimum age of OIB samples (Tables S1 and S2).

289 To estimate lithospheric thickness at the time of eruption for off-axis plumes, we
 290 assume that both the present-day lithospheric age (t_{crust}) and the OIB age (t_{OIB}) on each
 291 island follow a Gaussian distribution as

$$292 \quad t_{\text{crust}} \sim \mathcal{N}(\mu_1, \sigma_1^2), \quad (2)$$

$$293 \quad t_{\text{OIB}} \sim \mathcal{N}(\mu_2, \sigma_2^2), \quad (3)$$

294 where μ_1 is the oceanic crustal age, σ_1 is half of the age misfit, μ_2 is the mean of max-
 295 imum and minimum OIB eruption ages, and σ_2 is a quarter of the length of the OIB ma-
 296 jor eruption period. t_{crust} and t_{OIB} can be considered as independent random variables,
 297 thus the age of oceanic lithosphere at the time of OIB volcanism (t_{erupt}) should also fol-
 298 low a Gaussian distribution given by
 299

$$300 \quad t_{\text{erupt}} \sim \mathcal{N}(\mu_1 - \mu_2, \sigma_1^2 + \sigma_2^2). \quad (4)$$

301 Lithospheric thickness is estimated from the theoretical cooling models by assuming that
 302 it lies between the 1125 °C and 1225 °C isotherms. We assume that lithospheric thick-
 303 ness (z) at a given time follows a Gaussian distribution according to

$$304 \quad z \sim \mathcal{N}(\mu_3, \sigma_3^2), \quad (5)$$

305 in which μ_3 is the mean of the lithospheric thickness obtained from the 1125°C and 1225°C
 306 isotherms and σ_3 is a quarter of the difference in depth between them. For each island,

we randomly choose a t_{erupt} based on Equation (4) and calculate the corresponding lithospheric thickness using Equation (5). Iteratively repeating this process until reaching a stable distribution of thickness estimates yields the plate-model derived mean value of lithospheric thickness beneath each ocean island.

For the seismically constrained estimates of lithospheric thickness, we test two end-member scenarios: (i) lithospheric thickness at the time of eruption is equivalent to that of the present day; and (ii) following eruption and movement away from the location of the plume tail, the lithosphere has re-thickened to its present-day value in accordance with conductive cooling following a half-space model. The true scenario likely falls between these two assumptions. Both assumptions yield similar results, likely because the majority of OIBs in our dataset are young (< 10 Ma) and the lithosphere cannot substantially rethicken over such a short time frame. Correcting for this process makes no appreciable difference to our results (< 5 km thickness change; see Supplementary Tables S4 and S5) and the size of this correction is generally smaller than the depth range covered by the $1175 \pm 50^\circ\text{C}$ isotherms. When using seismically derived estimates of lithospheric thickness, we therefore adopt the first option above.

Estimated lithospheric thickness at the time of eruption, based on either the basin-specific plate models (Richards, Hoggard, Crosby, et al., 2020) or seismological constraints (Hoggard, Czarnota, et al., 2020), are tabulated in Supplementary Dataset Tables S4 and S5. Plate model thicknesses for the Atlantic basin are slightly greater than those derived from the global-average model, whereas in the Indian and Pacific basins, lithospheric thickness estimates from basin-based models are similar to, or thinner than, those of the global model (Supplementary Figure S1).

2.3 Bayesian Model Selection

To investigate the variation of each geochemical parameter with lithospheric thickness, we have plotted and parameterised OIB geochemical data against lithospheric thickness at the time of eruption. To understand whether a particular dataset suggests a trend, or a change in gradient, we make use of Bayes factors: the ratio of the evidence or marginal likelihood between two competing statistical models (Jeffreys, 1935; Kass & Raftery, 1995). The evidence represents the integral of the likelihood over the prior for a given model choice. In our case, it evaluates how likely it is to generate the observed geochemical dataset, based on a specified model. Therefore, given two or more competing models, the model with the larger evidence is preferred. Computing the evidence is difficult, particularly for large dimension models, but for this problem we use Dynamic Nested Sampling (Skilling, 2006; Speagle, 2020), which gives both posterior and evidence estimates in a single analysis.

The geochemical data include the raw and fractional crystallisation-corrected concentrations of major elements, trace elements and λ values calculated from REE concentrations. To determine whether a given geochemical parameter is sensitive to lithospheric thickness or influenced by any potential sudden changes in mantle composition, such as the phase change from spinel to garnet peridotite, three models were compared: (i) a constant value model (which would imply no sensitivity to lithospheric thickness and, thus, no lid effect); (ii) a linear model (which suggests a lid effect); and (iii) a bi-linear model that permits a change in gradient at some depth determined by the data (Figure 4). We choose not to examine exponential models since they are monotonous, so incapable of describing a reverse in a trend or detecting the depth of a potential trend change. To estimate posterior probability densities of the model parameters for each candidate model, we choose an independent Gaussian likelihood whose negative log is written as

$$L(\mathbf{p}|\mathbf{d}) = \sum_{i=1}^M \sum_{j=1}^{N_i} \frac{(p_i - d_j)^2}{\sigma^2}, \quad (6)$$

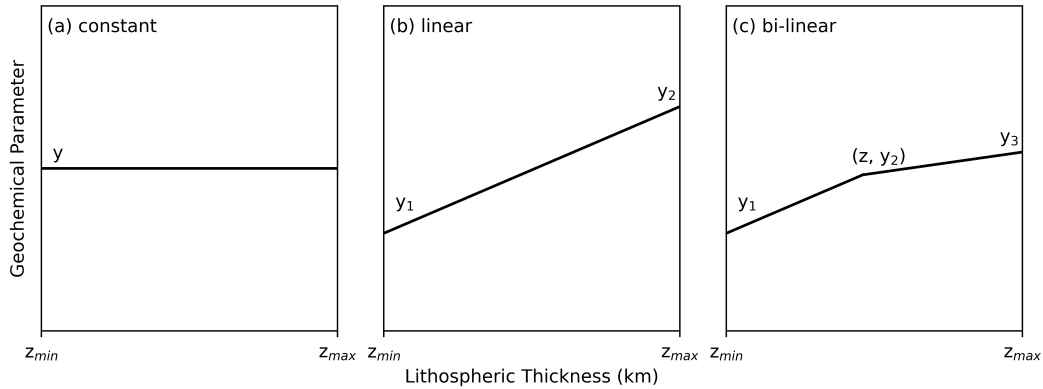


Figure 4. Schematic cartoon showing (a) a constant model with one unknown parameter (i.e. no lid effect); (b) a linear model with two unknown parameters; and (c) a bi-linear model with four unknown parameters. Associated model variables are labelled.

357 where M is the number of islands, N_i the number of samples for each island i , p_i is the
 358 model prediction of the geochemical concentration for island i , d_j is the observed data
 359 value for each sample from that island, and σ is the overall standard error. This formu-
 360 lation assumes that the data follows the standard normal distribution at each lithospheric
 361 thickness.

362 We fix values for the minimum and maximum lithospheric thicknesses (z_{min} and
 363 z_{max} in Figure 4), resulting in one, two and four unknown parameters for the constant,
 364 linear and bi-linear models, respectively. The use of Bayes factors to test the relative sup-
 365 port of competing models is subtly affected by the choice of priors. Regarding priors for
 366 the y values (i.e., the geochemical data), we adopt an empirical Bayes approach and set
 367 the prior to be Gaussian with mean and standard deviation equal to that of the over-
 368 all data. The mean and standard deviation of z (i.e., the lithospheric thickness of a pu-
 369 tative transition in the trend for the bi-linear model) are assumed to be 60 km and 5 km
 370 respectively, close to the average of all thickness data. To test the sensitivity of evidence
 371 calculations, we ran repeated tests that changed the standard deviation of the prior by
 372 $\pm 10\%$, which resulted in an average change of evidence values of ± 0.14 . Similarly, chang-
 373 ing the standard deviation by $\pm 50\%$ (a comparatively large change in the prior) resulted
 374 in an average change in the evidence of ± 0.18 . We are therefore confident that the choice
 375 of priors for our Bayesian evidence calculations are reasonable and that sensitivity to the
 376 choice of priors is minor. Nonetheless, in the Bayesian evidence results herein, a reason-
 377 able error bound on the numerical evidence values would be ± 0.2 .

378 The evidences for constant, linear and bi-linear models are denoted as E_0 , E_1 , and
 379 E_2 , respectively. Since evidence values are typically vanishingly small numbers, they are
 380 usually represented by their logarithms. A candidate model with a larger evidence value
 381 is to be preferred, for example, model “A” with a \log_{10} evidence of -1000 is a hundred
 382 times more likely than a competing model “B” with a \log_{10} evidence of -1002. Gener-
 383 ally a difference in the \log_{10} evidence greater than 2 is taken to be statistically signif-
 384 icant (Jeffreys, 1935; Kass & Raftery, 1995). As a reminder, the constant model implies
 385 that a geochemical parameter is insensitive to changes in lithospheric thickness. The lin-
 386 ear model can detect an overall trend, but is incapable of describing a change or rever-
 387 sal in trend. The bi-linear model can be useful for identifying a change point in a trend
 388 and even detecting a reversal of the trend, but is more sensitive to outliers. For a given
 389 geochemical parameter, if $\log_{10} E_1 - \log_{10} E_0 > 2$, we are confident in saying that it varies
 390 with lithospheric thickness. Furthermore, if $\log_{10} E_2 - \log_{10} E_1 > 2$, we can say that a

change-point or kink can be found in the data trend. In these cases, we provide histograms of the depth of the likely kink in the model and calculate its mean and standard deviation.

2.4 Sensitivity to Sites with Large Numbers of Samples

Due to the form of our likelihood function in Equation (6), clusters of large numbers of measurements from a single site could potentially bias the results. Two notable examples of this are the large OIB sample sizes of Iceland and Hawaii. To test the robustness of our results to potential biasing from these two localities, we repeat the calculation of posterior probability densities and evidence values for each geochemical parameter using: (i) all data (i.e. our reference case); and (ii) the dataset with samples from both Iceland and Hawaii excluded. Removal of Hawaiian samples is of particular relevance because they represent the only OIBs located on thick lithosphere that are dominated by tholeiites (e.g., MacDonald & Katsura, 1964). All other OIBs at and beyond these lithospheric thicknesses consist predominantly or exclusively of alkali basalts (e.g., Schmincke, 1982; Fisk et al., 1988; Gautier et al., 1990).

3 Results

To provide a relatively simple overview that gets at the essence of our results, we have chosen to focus in the main text on a preferred reference case. This case includes the initial correction of geochemical concentrations for the effects of fractional crystallisation, uses data from all OIB localities within our database, and adopts lithospheric thicknesses from basin-specific plate-cooling models. While we discuss any important differences that arise from changes to this reference setup in the main text, the full suite of associated figures and results are presented in the Supplementary Information.

3.1 Geochemical Histograms

Raw histograms of major element concentrations for all OIB data, prior to application of sample filters, display slightly skewed Gaussian distributions with peaks at approximately 7 wt.% for MgO, 48 wt.% for SiO₂, 3 wt.% for TiO₂, and 14 wt.% for Al₂O₃ (blue bars in Figure 5a–d). The MgO peak at 7 wt.% broadly coincides with the minimum in magma density at 7–8 wt.% MgO calculated using *Petrolog3* at 0.1 GPa, which is consistent with expectations that the lightest magmas are the most likely to erupt at the surface (see Supplementary Figure S2; Danyushevsky & Plechov, 2011). The continuous distribution of major element concentrations is consistent with expectations for mixing of distinct, end-member reservoirs to varying extents, which is also supported by isotopic evidence (e.g., Hart et al., 1992). Filtering the raw data according to the criteria outlined in Section 2.1.2 has limited impact on distributions for SiO₂, Al₂O₃ and TiO₂, but the filtered MgO histogram retains only the right-hand side of the distribution due to the sharp cut-off of samples with MgO < 7 wt.% (green bars in Figure 5a–d). Histograms of the REE shape parameters for filtered OIB samples exhibit more scatter and less clean unimodal behaviour (Figure 5e–g). Nevertheless, λ_0 has a clear peak at ~ 3.3 . λ_1 is left skewed, with a peak around 10 and more than 80% of samples have $\lambda_1 > 5$. λ_2 is somewhat bimodal, with a central peak at approximately -15 and a subsidiary peak at -40.

3.2 Evidence Results

3.2.1 Example of Statistical Results

To illustrate our procedure for quantifying the relationship between lithospheric thickness and various geochemical parameters, we present two examples for Al₂O₃ and

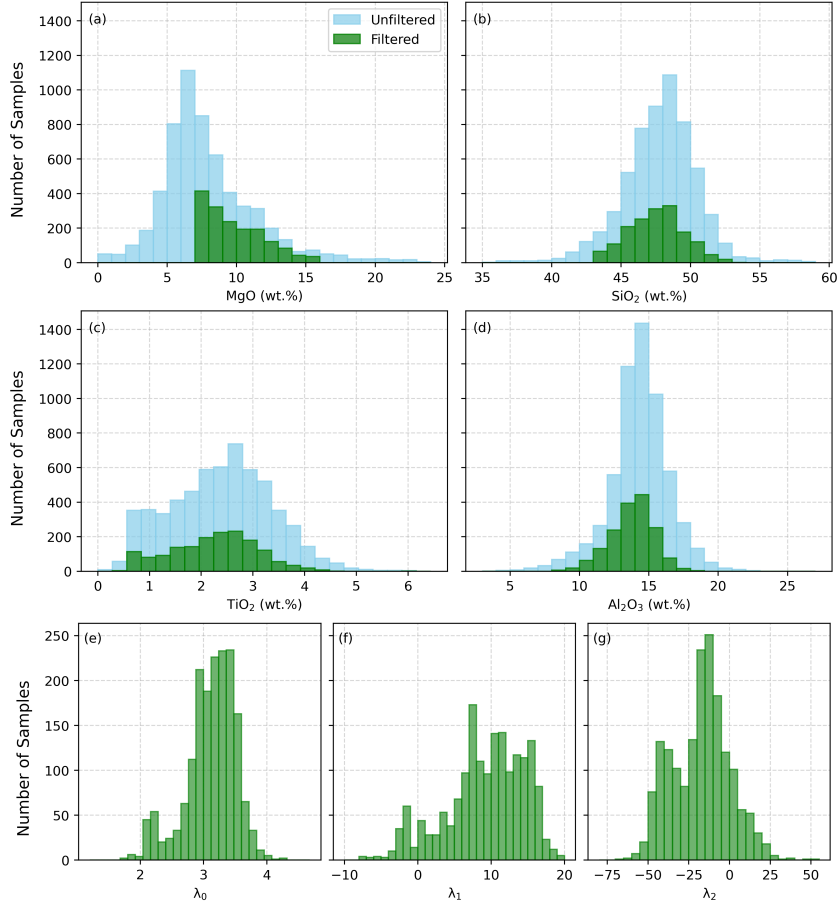


Figure 5. Concentration histograms of (a) MgO; (b) SiO₂; (c) TiO₂; and (d) Al₂O₃ in our OIB dataset. Original, unfiltered data are colored blue, while data in green represent the subset of data remaining following application of screening filters outlined in Section 2.1.2. For simplicity, histograms of (e) λ_0 , (f) λ_1 , and (g) λ_2 values are shown only for filtered OIB samples.

437 λ_1 in Figure 6. Both use our reference setup, in which the global OIB dataset is filtered
 438 and corrected for fractional crystallisation, with lithospheric thickness evaluated via the
 439 basin-specific plate model. Black crosses represent individual OIB samples and \log_{10} of
 440 the evidence is provided for each of the three types of model.

441 For both Al₂O₃ and λ_1 , we find that the evidence increases by ~ 160 when moving
 442 from constant to linear models (compare Figure 6a with 6b, and 6e with 6f), confirm-
 443 ing the existence of a lid effect for both Al₂O₃ and λ_1 . However, we see contrast-
 444 ing results when the bi-linear model is introduced. For Al₂O₃, evidence values for lin-
 445 ear and bi-linear models are similar (Figure 6b–c), implying the absence of any obvious
 446 transition in the trend as a function of lithospheric thickness. The resulting probabili-
 447 ty distribution of potential kink depths is therefore broad and poorly constrained in Fig-
 448 ure 6d, and we infer that Al₂O₃ in OIBs decreases linearly with increasing lithospheric
 449 thickness, with no definitive kink. On the other hand, λ_1 shows a clear preference for
 450 a bi-linear model, with an increase in the \log_{10} evidence value of ~ 87 over a linear model
 451 (Figure 6f–g). The associated probability distribution for the kink is tightly constrained
 452 in the depth range of 49–56 km, with an average of ~ 52 km (Figure 6h). Based on this
 453 preferred bi-linear model, the most likely trend for λ_1 is that it increases with lithospheric

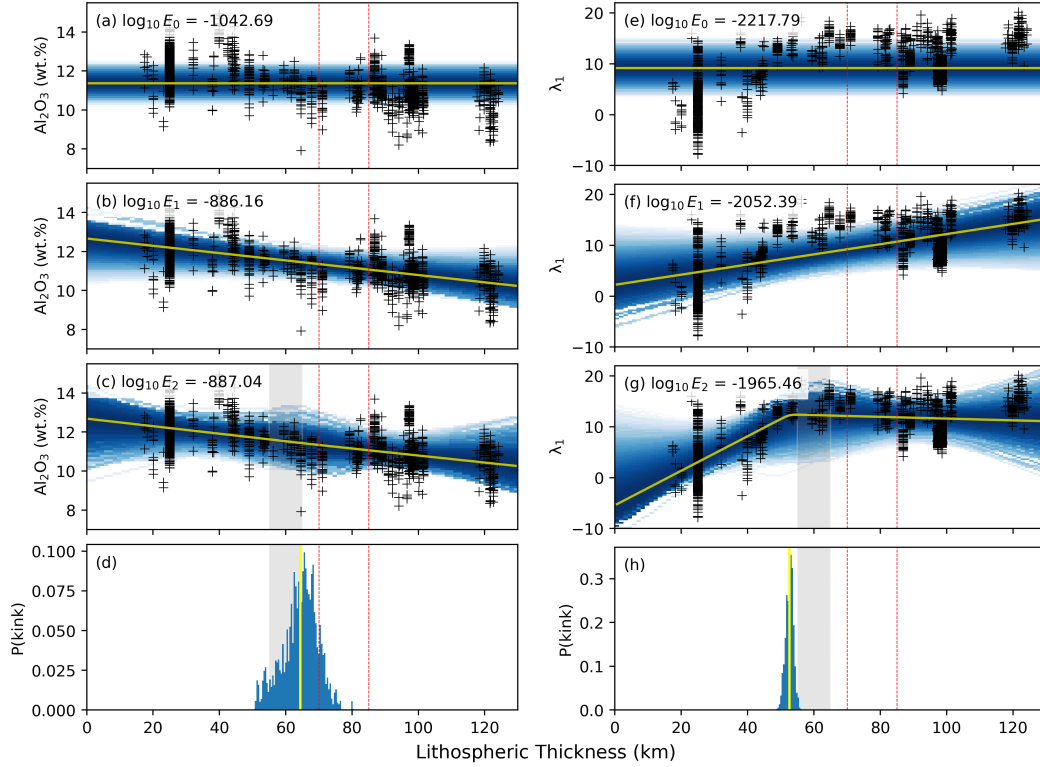


Figure 6. Statistical evidence evaluation results for Al_2O_3 and λ_1 under our reference setup. (a) Al_2O_3 as a function of lithospheric thickness fitted using a constant model; black crosses = individual samples; blue shading = probability density; yellow line = mean model; red dotted lines = expected spinel-garnet transition depths for typical mantle potential temperatures expected in plumes (e.g. Robinson & Wood, 1998; Klemme & O’Neill, 2000; Tomlinson & Holland, 2021); inset gives \log_{10} evidence value. (b) Same for a linear model. (c) Same for a bi-linear model; grey band = prior distribution for kink depth. (d) Probability distribution of kink depths; grey band = prior; blue histogram = posterior; yellow line = mean value. (e–h) Same as a–d, albeit for λ_1 .

454 thickness until a depth of ~ 52 km, before subsequently remaining approximately con-
 455 stant.

456 3.2.2 Summary of Evidence Evaluation Results

457 Values of $\log_{10}E_1 - \log_{10}E_0$ and $\log_{10}E_2 - \log_{10}E_1$ have been determined for each
 458 geochemical parameter, under our reference setup. As a reminder, when greater than a
 459 key threshold value of two (i.e. more than hundred-fold increase in the likelihood), the
 460 former indicates statistical preference for a linear model over a constant one, while the
 461 latter indicates a bi-linear rather than linear relationship.

462 The preferred model for each geochemical parameter is shown in Figure 7, with fur-
 463 ther details in Figures 8–11, and can be summarised as follows:

- 464 1. All geochemical parameters prefer either a linear or bi-linear model over a con-
 465 stant model, indicating universal sensitivity to lithospheric thickness.

Constant																		
Linear						✓	✓	✓			✓	✓					✓	
Bi-linear	✓	✓	✓	✓	✓				✓	✓			✓	✓				
	CaO	K ₂ O	Na ₂ O	P ₂ O ₅	TiO ₂	SiO ₂	Al ₂ O ₃	FeO	La	Th	Yb	Lu	λ ₀	λ ₁	λ ₂			

Figure 7. Optimal model type for each geochemical parameter under our reference setup. Ticks denote optimal model; strength of colour fill indicates level of preference for that model type (i.e., when a simpler model has an evidence value that is within 20 but less than 2 of the optimal model, it is filled with colour that linearly increases in intensity).

- 466 2. For major elements Al₂O₃, FeO, and SiO₂, data are optimally fitted by linear mod-
 467 els (Figure 8). Conversely, TiO₂, Na₂O, K₂O, CaO, and P₂O₅ data are optimally
 468 fitted by bi-linear models (Figure 9c–g);
 469 3. For trace elements, the highly incompatible elements La and Th are best fitted
 470 by bi-linear models (Figure 9a–b), whereas the less incompatible Yb and Lu are
 471 best fitted by linear models (Figure 10);
 472 4. For parameters describing REE patterns, λ₀ and λ₁ are optimally fitted by bi-linear
 473 models (Figure 11a–b), whereas λ₂ prefers a linear model (Figure 11c).
 474 5. For geochemical parameters that prefer a bi-linear model, kink depths generally
 475 occur at lithospheric thicknesses of 50–60 km.

476 4 Discussion

477 4.1 Existence of a Lid Effect

478 Lithospheric thickness dictates the minimum pressure of plume melting through
 479 the so-called ‘lid effect’. It affects OIB chemistry in two ways (e.g., Watson & McKen-
 480 zie, 1991; Humphreys & Niu, 2009; Niu, 2021). First, by inhibiting upwelling beyond a
 481 certain depth, lithospheric thickness limits the maximum melt fraction (F). We there-
 482 fore expect F to be inversely proportional to lithospheric thickness, which will have a
 483 substantial impact on the concentrations of highly incompatible trace elements. Second,
 484 the pressure at which melting occurs has strong implications for the mineral phases present
 485 in the residue following partial melting. In particular, over the depth range of interest
 486 here, the stable aluminium-rich phase converts from garnet (Mg₃Al₂Si₃O₁₂) to spinel (MgAl₂O₄)
 487 with decreasing pressure, subsequently becoming plagioclase (CaAl₂Si₂O₈) at shallow depths
 488 beneath mid-oceanic spreading centers (e.g., Masaaki, 1980). Despite our analyses be-
 489 ing subject to uncertainty, particularly in relation to estimates of lithospheric thickness
 490 and assumptions on uniform source composition, the data support a linear or bi-linear
 491 trend between all geochemical parameters and lithospheric thickness, providing univer-
 492 sal evidence for the lid effect and corroborating the conclusions of, for example, Humphreys
 493 and Niu (2009), Dasgupta et al. (2010) and Niu (2021).

494 Nonetheless, it is clear from our results that different geochemical parameters ex-
 495 hibit distinct responses to the lid effect. Some trends (e.g., Al₂O₃) show a linear rela-
 496 tionship with lithospheric thickness, whereas others show a bi-linear relationship with
 497 an abrupt change at a certain depth (e.g., λ₀, λ₁). In the following sections, we discuss
 498 potential explanations for these behaviours. We start with major element trends that
 499 are best fitted by linear models, with an emphasis on the relationship to pressure-dependent

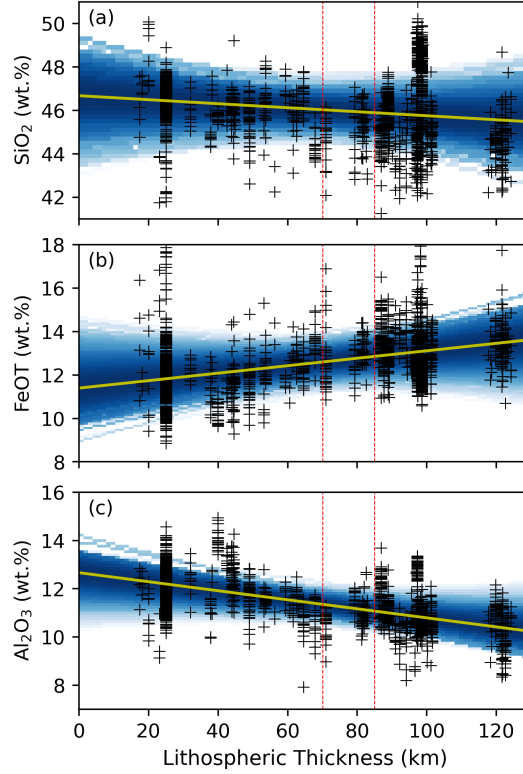


Figure 8. Statistical evidence evaluation results for major elements optimally fitted by linear models, under our reference setup. (a) Results for SiO_2 for all localities; black crosses = individual samples; blue shading = probability density; yellow line = mean model; red dotted lines = spinel-garnet transition depths (e.g., Robinson & Wood, 1998; Klemme & O’Neill, 2000; Tomlinson & Holland, 2021). (b) Same for FeOT. (c) Same for Al_2O_3 .

500 mineral assemblages. We then discuss the remaining major and trace elements, relat-
 501 ing observed trends to the influence of variations in melt fraction and the spinel-garnet
 502 phase transition. Although Yb and Lu are best fitted by linear models, we include them
 503 in this section because their behaviour is associated with an interplay between F and
 504 the spinel-garnet phase transition. We finish by discussing REE trends, described by λ_i ,
 505 drawing on the lessons learned from interpretation of trace elements trends.

506 4.2 Major Elements with Linear Trends

507 Concentrations of the major elements SiO_2 , FeOT and Al_2O_3 in OIBs show a linear
 508 dependence on lithospheric thickness (Figure 8). In mantle melts, these components
 509 are known to be buffered by the mineral assemblage of the mantle residue and the ob-
 510 served trends are consistent both with experimental studies on the Calcium, Magnesium,
 511 Aluminium, Silicon (CMAS) system (e.g., Walter & Presnall, 1994) and with the results
 512 of previous observational studies (e.g., Humphreys & Niu, 2009; Niu et al., 2011; Niu,
 513 2021).

514 SiO_2 exhibits a moderate decrease with increasing lithospheric thickness (Figure
 515 8a). Its concentration in mantle melts is buffered by the two most abundant minerals
 516 in the upper mantle, olivine and orthopyroxene, according to the reaction



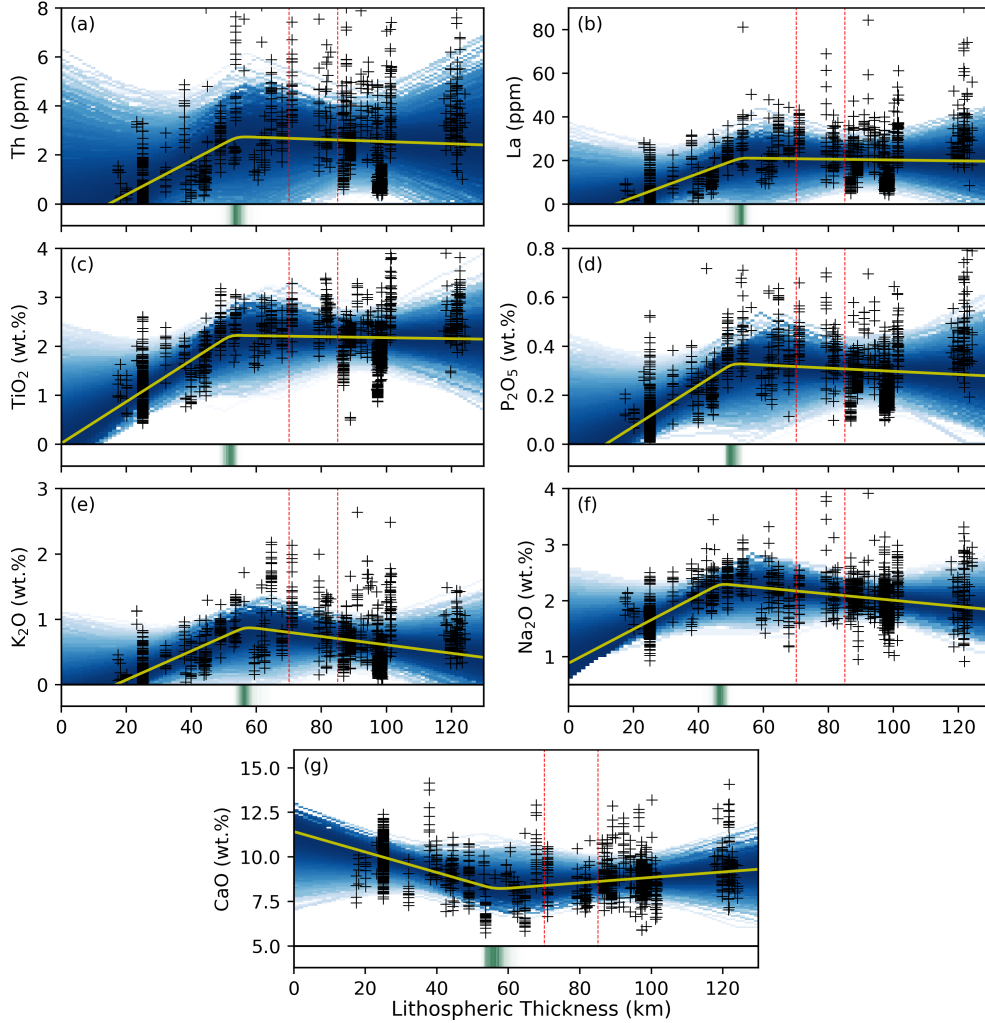


Figure 9. Statistical evidence evaluation results for geochemical parameters optimally fitted by bi-linear models. Data and panel contents same as for Figure 8 but for (a) Th, (b) La, (c) TiO_2 , (d) P_2O_5 , (e) K_2O , (f) Na_2O , and (g) CaO . The horizontal bar below panel (d) shows the probability distribution of the likely kink depth, with more opaque colors indicating that a kink is more likely at that depth.

518 Increasing pressure drives this reaction to the right, expanding the stability field of or-
 519 thopyroxene at the expense of olivine (e.g., Campbell & Nolan, 1974; Walter & Presnall,
 520 1994). As a consequence, as the average melting pressure increases beneath thicker litho-
 521 sphere, the residue contains more SiO_2 -rich orthopyroxene and the corresponding melts
 522 produced are increasingly SiO_2 -poor (e.g., Bohlen et al., 1980; Bohlen & Boettcher, 1981).
 523 We note that Herzberg (1992) further proposed that the decrease in SiO_2 with increas-
 524 ing melt pressure stops at ~ 45 wt.% SiO_2 due to low melt fractions in the presence of
 525 garnet, but this cut-off behaviour is not observed in either our analyses or in previous
 526 studies (e.g., Scarrow & Cox, 1995; Dasgupta et al., 2010). We therefore suggest that
 527 the spinel-garnet transition has limited influence on the SiO_2 content of OIBs, with re-
 528 action (7) and associated buffering of the silica content by olivine and orthopyroxene be-
 529 ing the key control.

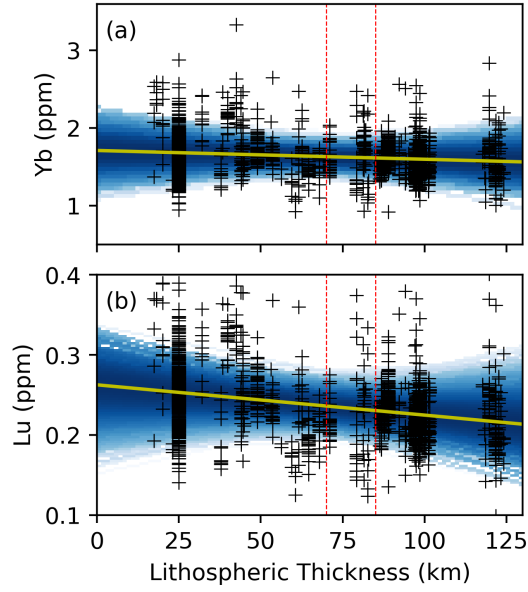


Figure 10. Statistical evidence evaluation results for HREEs, which are optimally fitted by linear models. Data and panel contents same as for Figure 9 but for (a) Yb and (b) Lu.

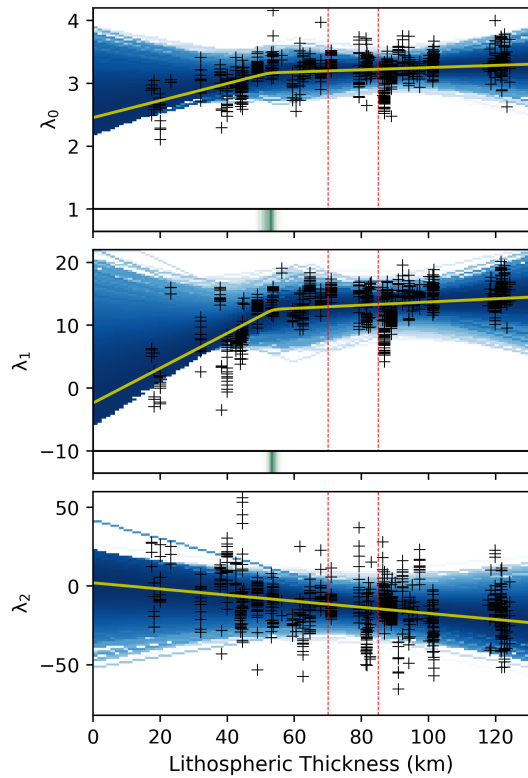


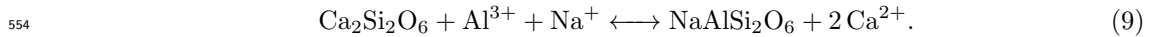
Figure 11. Statistical evidence evaluation results for REE shape parameters. Data and panel contents same as for Figure 9, but for (a) λ_0 , (b) λ_1 and (c) λ_2 . Note that λ_0 and λ_1 are optimally fitted by bi-linear models, whereas λ_2 is optimally fitted by a linear model.

530 We also attribute the linear increase in FeOT with increasing lithospheric thick-
 531 ness (Figure 8b) to the relative stabilities of olivine and orthopyroxene as a function of
 532 pressure. Olivine contains more Fe than orthopyroxene and increasing the pressure sta-
 533 bilizes orthopyroxene at the expense of olivine. As a consequence, for similar melt frac-
 534 tions, high-pressure melts contain more Fe than low-pressure melts. The relative abun-
 535 dance of olivine and orthopyroxene in the residue was also used by Niu (2016) to explain
 536 the increase in FeOT in mid-ocean ridge basalts (MORB) with increasing ridge axial depth.
 537 Analysis of our OIB dataset demonstrates that this trend can be extended over a greater
 538 depth range than is possible with the MORB data alone.

539 Al_2O_3 linearly decreases with increasing lithospheric thickness (Figure 8c), which
 540 we believe can be attributed to an increase in the Al content of clinopyroxene and, to
 541 a lesser extent, orthopyroxene, with increasing pressure. Al^{3+} can occupy either the tetra-
 542 hedral or octahedral sites within the pyroxene crystal lattice. The two tetrahedral sites
 543 are characterised by a central cation (usually Si^{4+}) surrounded by four oxygen atoms,
 544 whereas the two larger octahedral sites are positions in which the central cation is sur-
 545 rounded by six oxygen atoms and are usually occupied with cations that have greater
 546 ionic radii, such as Ca^{2+} . Increasing pressure shrinks the octahedral M1 and M2 sites
 547 in both pyroxenes and allows more Al^{3+} to enter the M1 site, which is the smaller of the
 548 two octahedral sites (Colson & Gust, 1989). The octahedral Al^{3+} can either be charge
 549 balanced by additional Al^{3+} replacing Si^{4+} in an adjacent tetrahedral site according to
 550 the reaction



552 or by Na^+ or K^+ replacing a divalent ion on the larger M2 site (Campbell & Borley, 1974;
 553 Safonov et al., 2011), according to reaction



555 As a consequence, the Al_2O_3 content of the residual pyroxenes increases with increas-
 556 ing pressure and the Al_2O_3 concentration in the melt correspondingly decreases. This
 557 simple interpretation may be complicated, however, by Al^{3+} being buffered by reactions
 558 between spinel and pyroxene in the spinel stability field and between garnet and pyrox-
 559 ene in the garnet stability field. We might therefore have also expected a dependence
 560 on the spinel-garnet transition. The fact that our Al_2O_3 trends do not require a bi-linear
 561 model in our reference setup suggests that this is not the case, perhaps because both spinel
 562 and garnet contain two Al^{3+} ions and the increasing Al content of pyroxenes with pres-
 563 sure is therefore not affected by the spinel-garnet transition.

564 In summary, we infer that variations in the concentration of major elements SiO_2 ,
 565 FeOT, and Al_2O_3 in OIBs are dominated by gradual changes in mineral assemblage as
 566 a function of pressure rather than variations in F or effects arising from the spinel-garnet
 567 phase transition.

568 4.3 Major and Trace Elements with Bi-linear Trends

569 The behavior of trace elements, which do not form stoichiometric components in
 570 minerals, can be understood using the distribution coefficient, D , for the partitioning of
 571 the element between a mineral and the melt. During partial melting of a mantle peri-
 572 dotite, the concentration of a given element in the aggregate melt (C_1) during batch melt-
 573 ing is given by

$$574 \quad C_1 = \frac{1}{D'(1-F) + F} C_s, \quad (10)$$

575 and, in the case of fractional melting, is

$$576 \quad C_1 = \frac{1}{F} \left[1 - (1-F)^{\frac{1}{D'}} \right] C_s, \quad (11)$$

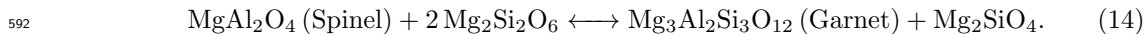
577 where D' is the bulk partition coefficient, F is the melt fraction and C_s is the concen-
 578 tration of the element in the source prior to melting (Shaw, 1970, 1979). C_1 is therefore
 579 controlled by the combined effect of D' and F . Nevertheless, for incompatible trace el-
 580 ements where D' is low (usually < 0.01), these equations can be simplified to

$$581 \quad C_1 \approx \frac{1}{F} C_s, \quad (12)$$

582 indicating that C_1 is proportional to $\frac{1}{F}$, irregardless of the melting mechanism. The lower
 583 the value of D' , the more reliable this approximation becomes. Similarly for moderately
 584 low values of D' (i.e. < 0.2), given that melt fractions for OIBs are never higher than
 585 ~ 0.2 , we can simplify Equations (10) and (11) to

$$586 \quad C_1 \approx \frac{1}{D' + F} C_s. \quad (13)$$

587 In cases where $D' > 0.2$ and differences in the partition coefficients for different
 588 minerals are large, which can occur, for example, across the spinel-garnet phase tran-
 589 sition, C_1 is influenced by both pressure and the phase change. The case of spinel-garnet
 590 can be represented by a reaction between spinel and pyroxene to give garnet and olivine
 591 according to



593 The transition is abrupt and temperature dependent (e.g. Klemme & O'Neill, 2000). For
 594 temperatures appropriate for mantle plumes, the transition occurs over a ~ 5 km depth
 595 range somewhere between 70–85 km, depending on the mantle composition (e.g. Robin-
 596 son & Wood, 1998; Klemme & O'Neill, 2000; Wood et al., 2013; Tomlinson & Holland,
 597 2021). Note that the shallower plagioclase-spinel transition in peridotite is not relevant
 598 to this study because the plagioclase stability field extends only to pressures of 0.8 GPa
 599 in fertile lherzolite and to 0.6 GPa in depleted lherzolite, corresponding to depths of 24 km
 600 and 18 km, respectively (Borghini et al., 2010).

601 For geochemical parameters that are best fitted by bi-linear models, we divide them
 602 into two groups: (i) elements exhibiting low partition coefficients ($D' < 0.2$), includ-
 603 ing Th, La, Ti, P, K and Na, which we propose can be interpreted primarily in terms
 604 of melt fraction F (although Na and K may be further influenced by D values for py-
 605 roxenes at high pressure); and (ii) Ca, which requires consideration of both F and the
 606 spinel-garnet phase change. These bi-linear trends were not identified in previous stud-
 607 ies (e.g., Ellam, 1992; Humphreys & Niu, 2009; Dasgupta et al., 2010; Niu et al., 2011;
 608 Niu, 2021) and we discuss their likely origin.

609 **4.3.1 Incompatible elements**

610 D' values for the incompatible elements investigated in this study decrease in the
 611 following order: $\text{Ti} \approx \text{P} \approx \text{Na} > \text{La} > \text{K} > \text{Th}$. All are optimally fitted by bi-linear mod-
 612 els, in which their concentrations initially increase rapidly with increasing lithospheric
 613 thickness, before remaining flat or increasing at a significantly reduced rate in the cases
 614 of Th, La, Ti, P, or slightly decreasing in the cases of K and Na. The kinks in slopes all
 615 occur at 50–60 km depth (Supplementary Figure S3).

616 La, K and Th are highly incompatible in peridotites, regardless of whether the ma-
 617 jor aluminum-rich phase is spinel or garnet ($D' \leq 0.01$; Table 1). Following on from
 618 our interpretation of Equations (10) and (11) for such elements, at constant potential
 619 temperature, we expect variations in their concentration to be proportional to $\frac{1}{F}$ as a
 620 function of lithospheric thickness and insensitive to the spinel-garnet phase transition
 621 (dashed line in Figure 12a). This behaviour should impart an increase in incompatible
 622 trace element concentrations at larger thicknesses, with a steeper rate of increase at higher

Table 1. Partition coefficients for incompatible elements in the main peridotite minerals. D'_{sprd} and D'_{gprd} are bulk partition coefficients for spinel peridotite (assuming model abundances of 59% Ol, 28% Cpx, 8% Opx, 5% Sp) and garnet peridotite (55% Ol, 23% Cpx, 15% Opx, 7% Grt), respectively. D in each mineral can vary as a function of mineral composition, temperature and pressure.

	Ol	Opx	Cpx	Sp	Grt	D'_{sprd}	D'_{gprd}
Th	0.0001	0.0001	0.00026	0.00001	0.0001	0.00014	0.00014
K	0.00018	0.001	0.002	0.0001	0.001	0.00075	0.00078
La	0.0004	0.002	0.054	0.01	0.01	0.016	0.014
Ti	0.02	0.1	0.18	0.15	0.28	0.078	0.087
P	0.1	0.03	0.05	0	0.1	0.075	0.078
Na	0.006	0.05	0.2	0	0.04	0.064	0.060
Lu	0.0015	0.06	0.28	0.01	7.7	0.085	0.61
Yb	0.0121	0.1036	0.5453	0.01	6.9	0.17	0.63

623 thicknesses. This prediction is consistent with the observed increase in incompatible el-
 624 element concentrations with increasing lithospheric thickness beneath thinner lithosphere.
 625 When lithospheric thickness exceeds 50–60 km, however, it is not consistent with the marginally
 626 increasing, flat or decreasing concentrations observed. We can further demonstrate this
 627 aspect by converting our observed concentrations of La into estimates of F as a func-
 628 tion of lithospheric thickness (solid purple line in Figure 12a) and comparing them to
 629 the predicted F curves (note that the resulting F curve is insensitive to the choice of La
 630 or Th). There is an agreement between the shapes of the two curves below a lithospheric
 631 thickness of ~ 30 km but they become inconsistent at larger thicknesses, implying that
 632 another process modulates concentrations of incompatible elements beyond thicknesses
 633 of ~ 55 km.

634 The moderately incompatible elements Na, P and Ti have $D' \sim 0.06 - 0.08$ in
 635 both the spinel and garnet stability fields and follow similar trends. For these elements,
 636 D' cannot be neglected and Equation (13) should be used to interpret changes in their
 637 concentrations. Since D' varies little with mineralogy for these elements, it can be re-
 638 garded as a constant and F becomes the dominant variable. As a consequence, exper-
 639 imental and theoretical constraints imply that these moderately incompatible element
 640 concentrations should again increase with increasing lithospheric thickness, with steeper
 641 rates of increase at greater thicknesses. The contribution from D' should reduce the ef-
 642 fect of F , diluting the concentration ratio of these elements between the melts and residue
 643 at higher pressures without altering the underlying trend. This prediction is consistent
 644 with observations for lithospheric thicknesses less than 55 km, but it is inconsistent with
 645 thicker lithosphere trends, which again suggest minimal changes in F at larger thicknesses.

646 Our analyses demonstrate that the concentrations of Na and K differ from other
 647 incompatible elements in that they show a slight decrease with increasing lithospheric
 648 thickness beyond the kink (Figure 9e and f). At these pressures, F is expected to be small
 649 and to decrease with increasing lithospheric thickness. The observed trends in Na and
 650 K may therefore indicate that variations in D' are playing a role. As discussed in Sec-
 651 tion 4.2, increasing pressure allows entry of Al^{3+} into the clinopyroxene M1 site. Via re-
 652 action (9), this substitution can be charge balanced by replacing a X^{2+} cation in the larger
 653 M2 site with Na^+ and/or K^+ , resulting in an increase of D' for K^+ and Na^+ with in-
 654 creasing pressure. This effect may explain their observed decrease in concentration with
 655 increasing lithospheric thickness, although we note that Na^+ is expected to have a stronger
 656 affinity for the M2 site than K^+ because its ionic size is closer to the preferred size of
 657 the site (Safonov et al., 2011).

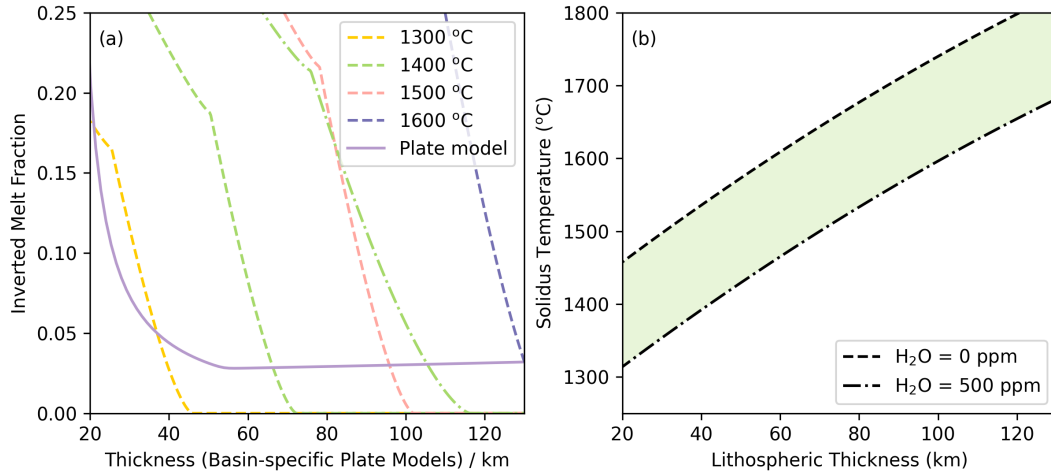


Figure 12. (a) Solid line = melt fraction as a function of lithospheric thickness inferred from Equation (10) and the bi-linear trends for La concentrations, with basin-specific plate model derived estimates of lithospheric thickness; dashed lines = theoretical melt fraction for decompression melting of dry, primitive peridotite at different potential temperatures from the parameterisation of Katz et al. (2003), as modified by Ball et al. (2022); dash-dotted line = same for a wet 1400°C source with H₂O = 500 ppm, which is thought to be an upper bound for water content in plume source regions (e.g., Wallace, 1998; Asimow & Langmuir, 2003). (b) Solidi for peridotite with 0–500 ppm water contents.

658

4.3.2 CaO

659

660

661

662

663

664

665

666

667

668

669

670

671

672

673

674

675

676

Calcium is the element most likely to be affected by the spinel-garnet transition because garnet contains stoichiometric Ca, whereas spinel does not. The principal repositories for Ca²⁺ in garnet peridotites are, in order of decreasing affinity, clinopyroxene > garnet > orthopyroxene > olivine. Beneath shallow lithosphere, there is a steady decrease in CaO concentration with increasing lithospheric thickness up to ~55 km (Figure 9m–n). We attribute this behaviour to the continuous decrease in F , previously deduced from analyses of incompatible element trends: as F decreases, lower quantities of clinopyroxene are melted and the resulting melts have lower Ca concentrations. Our interpretation of the incompatible element trends suggests that, beyond the kink, F should remain approximately constant or continue to decrease, but at a reduced rate. Therefore, we would expect a further decrease in CaO (albeit at a lower rate), rather than the increase that is observed. The cause of this increase is unclear, but assuming that F is not changing (as suggested by the most incompatible elements), it requires that, with increasing pressure, a Ca-rich phase (presumably Ca-rich pyroxene) is melting in preference to moderately Ca-poor garnet and orthopyroxene. We highlight that previous studies, which applied linear regression to the data, found no discernible trend between CaO and lithospheric thickness (e.g., Humphreys & Niu, 2009), likely because the reversal in trends from decreasing to increasing CaO counteract each other.

677

4.3.3 Yb and Lu

678

679

680

Concentrations of Yb and Lu change little with increasing lithospheric thickness, showing only a slight, linear decrease (Figure 10). This behaviour occurs despite the fact that these elements exhibit an order of magnitude difference in compatibility between

681 spinel (incompatible) and garnet (compatible; Table 1), from which we might expect to
 682 see a kink in their trends.

683 Within the spinel stability field, the decrease in F with increasing pressure (required
 684 by observed trends for incompatible trace elements) is offset by increasing D' due to an
 685 increasing amount of clinopyroxene in the residue at higher pressures (e.g., Green & Ring-
 686 wood, 1967). Within the garnet stability field, the constant or slight decrease in F with
 687 increasing lid thickness is initially offset by an increase in D' as garnet replaces spinel
 688 and, subsequently, as pressure continues to increase, by garnet partially replacing py-
 689 roxene according to reaction (14).

690 Superimposed on these changes is migration of low Yb-Lu melt from the garnet field
 691 into the spinel field, where it partially offsets the potential increase in the concentration
 692 of these elements due to their lower D' in the spinel field. This behaviour is termed the
 693 ‘memory effect’, whereby erupted melts preserve a geochemical signature of high-pressure
 694 melting despite the continuation of melting at shallower depths (e.g. Elliott et al., 1991).
 695 Taken together, this result implies that the absence of a kink in these trends derives from
 696 a combination of the spinel-garnet phase transition and the memory effect.

697 4.4 Shape of REEs

698 We next discuss the shape parameters, λ_i , for REE concentration patterns (O’Neill,
 699 2016). λ_0 is the average of the logarithmic concentration of all REEs except Eu, normalised
 700 by each element’s concentration in chondrites. Increasing lid thickness reduces the melt
 701 fraction, thereby more strongly elevating the concentration of highly incompatible LREEs
 702 (Figure 9) while having limited effect on the concentration of HREEs (Figure 10). It is
 703 therefore unsurprising that λ_0 follows trends defined by the highly incompatible elements,
 704 with a kink at ~ 55 km (Figures 11a).

705 λ_1 measures enrichment of LREEs with respect to HREEs and has a bi-linear trend,
 706 similar to λ_0 (Figure 11b). Previous studies described variations in REE trends using
 707 ratios, such as La/Yb and Sm/Yb, and related observed changes to an increasing abun-
 708 dance of garnet in the residue as melting pressures increase (e.g., Ellam, 1992; Humphreys
 709 & Niu, 2009). Nevertheless, these studies did not recognise either a kink or the influence
 710 of changes in F on LREE and, hence, the slope of the REE pattern. As noted in con-
 711 nection with λ_0 , the LREEs initially increase with increasing lithospheric thickness to
 712 ~ 55 km (Section 4.3.1), driven by changes in F , then remain nearly constant, while HREE
 713 concentrations change little throughout (Section 4.3.3). Therefore, the combined behaviour
 714 of LREEs and HREEs accounts for the observed variation in λ_1 .

715 λ_2 quantifies the curvature of the REE pattern, being positive if amphibole remains
 716 in the residue following melting and negative if garnet remains. OIBs are relatively dry,
 717 so amphibole is not expected to play a role in their genesis (e.g., O’Neill, 2016). Figure
 718 11c shows that the λ_2 trend is negative and linearly decreases with increasing lithospheric
 719 thickness, requiring increasing involvement of garnet and consistent with expectations
 720 (Figure 17 in O’Neill, 2016). Although there are some positive λ_2 values for melts pro-
 721 duced beneath thin lithosphere where garnet is not stable, the majority are negative and
 722 the trend becomes increasingly negative as the lithosphere thickens. This relationship
 723 provides further support for the memory effect (Elliott et al., 1991).

724 4.5 Trend Robustness

725 To analyse the robustness of our results to initial OIB processing steps, potential
 726 bias towards heavily sampled localities, and/or choice of lithospheric thickness model,
 727 we evaluate Bayes factors for a suite of additional scenarios including: (i) filtered OIB
 728 data prior to- and post-corrections for fractional crystallisation; (ii) datasets where Ice-
 729 land and Hawaii samples are included/excluded; and (iii) lithospheric thickness obtained

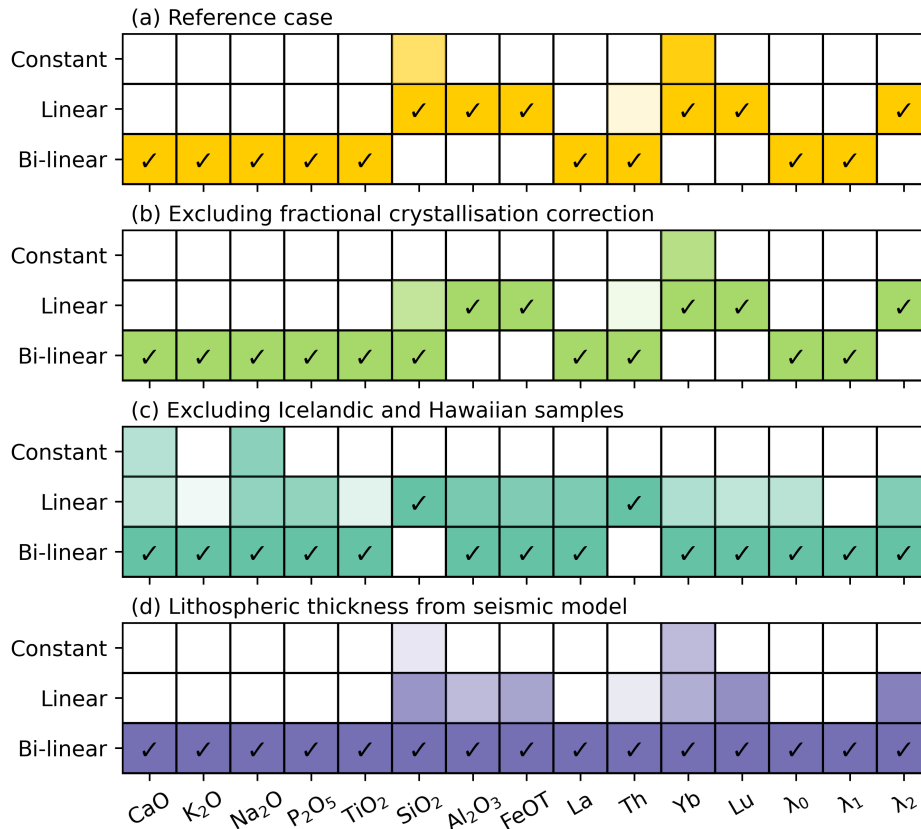


Figure 13. (a) Optimal model type for each geochemical parameter under our reference setup (filtered OIB samples from all localities corrected for fractional crystallisation, with lithospheric thicknesses from basin-specific plate-cooling models; as in Figure 7). (b) Same as reference setup except data are not corrected for fractional crystallisation. (c) Same as reference setup except Icelandic and Hawaiian samples excluded. (d) Same as reference setup albeit with lithospheric thickness taken from the model based on seismic tomography.

730 from the basin-specific plate-cooling models versus a model derived from seismic tomog-
 731 raphy. A summary of these results are presented in Figure 13, with further plots pre-
 732 sented in Supplementary Figures S4–S5.

733 4.5.1 Correction for Fractional Crystallisation

734 Our reverse-fractionation calculations in Petrolog3 suggest that primitive OIB melts
 735 commonly undergo 5–25% fractional crystallisation in the magma chamber (Supplemen-
 736 tary Figure S6). Correcting for fractional crystallisation does alter absolute geochem-
 737 ical concentrations, but the preference for a linear over constant dependence on litho-
 738 spheric thickness remains unchanged for all major and minor elements, and REE shape
 739 parameters (Figure 13b). In most cases, the preference for either linear or bi-linear mod-
 740 els also remains unchanged, the exception being SiO₂, for which the non-corrected data
 741 shows a preference for a bi-linear model. This behaviour is a direct consequence of im-
 742 posing the SiO₂ > 43 wt.% filtering criteria: for the non-fractionation corrected data,
 743 this results in a hard cut-off of all data below this value and preferentially increases pre-
 744 ferred model values in thicker lithosphere, whereas following fractionation correction, the

kink is smoothed out and SiO_2 linearly decreases with increasing lithospheric thickness (Supplementary Figures S7 and S8).

4.5.2 *Heavily Sampled Localities*

Hawaii and Iceland are heavily sampled in comparison to other localities in our OIB database, yielding high-density data clusters that may potentially introduce bias into the results. Nevertheless, we find that excluding these sites does not generally alter evidence in favour of the lid effect. For all geochemical parameters, there is still strong preference for either a linear or bi-linear model over a constant one. The two exceptions occur for Ca and Na, where the evidence with respect a constant model is still greater than 2 but less than 20 (Figure 13c).

With regards to preference for a bi-linear versus linear fit, removal of these localities has more of an influence on results. For geochemical parameters where all sites are optimally fitted by bi-linear models, excluding Iceland and Hawaii can either increase or reduce values of $\log_{10}E_2 - \log_{10}E_1$, depending on the parameter (Supplementary Figure S4a and e). In general, more parameters transition to preferring a bi-linear model (e.g., Al_2O_3 , FeOT, Yb, Lu and λ_2), with Si maintaining preference for a linear model and only Th switching from a bi-linear to linear model. This indicates that evidence in favour of bi-linear trends is not attributable to potential sampling bias from Hawaii and Iceland.

Nevertheless, it is interesting to note that excluding Icelandic and Hawaiian samples has an impact on the slope of the trend in thick lithosphere (beyond the kink depth of ~ 55 km). For incompatible elements Th, La, TiO_2 and P_2O_5 , the slope after the kink increases (Supplementary Figure S9), which is also the case for λ_0 and λ_1 (Supplementary Figure S10), albeit still at a lower rate than would be expected from theoretical arguments for melting at constant potential temperature and composition. For Na_2O and K_2O , it reduces the rate of concentration decrease with increasing lithospheric thickness (Supplementary Figure S9). All of these differences can likely be attributed to the concentrations of incompatible elements in Hawaiian basalts being lower than those of other OIBs on lithosphere of similar thickness. As noted in Section 2.4, Hawaiian basalts are dominated by tholeiites, whereas all other OIBs on thick lithosphere have alkali basalt affinities. Tholeiites are produced by higher degrees of partial melting (e.g., Yoder Jr & Tilley, 1962) and concentrations of incompatible elements are therefore expected to be diluted, which is consistent with the Hawaiian plume being hotter and stronger than other plumes beneath thick lithosphere (e.g., Hoggard, Parnell-Turner, & White, 2020). Hawaiian OIBs may also originate from a source that is more depleted in highly incompatible elements if, as suggested by Hofmann and Jochum (1996) and Pietruszka et al. (2013), it contains a significant amount of recycled oceanic gabbro. Regardless of the exact nature of the Hawaiian plume, its distinctive characteristics, coupled with the large number of samples available, can influence the slope of geochemical trends in thick lithosphere but does not refute evidence for the lid effect.

4.5.3 *Alternative Estimates of Lithospheric Thickness*

As introduced in Section 2.2, a limitation of theoretical cooling models is that they cannot capture local deviations in lithospheric thickness away from the average value for ocean floor of a given age (e.g., D. R. Davies et al., 2019). By comparing expected values with local estimates obtained from seismological constraints, we demonstrate that there are systematic differences between the two at the sites of OIBs in our database (Figure 14). For ocean islands on lithosphere younger than ~ 30 Ma, such as at Easter Island or the Azores, seismically inferred estimates of local lithospheric thickness systematically exceed expectations from plate-cooling models. This offset is likely artificial, being a consequence of surface wave tomography having limited resolution at depths shall-

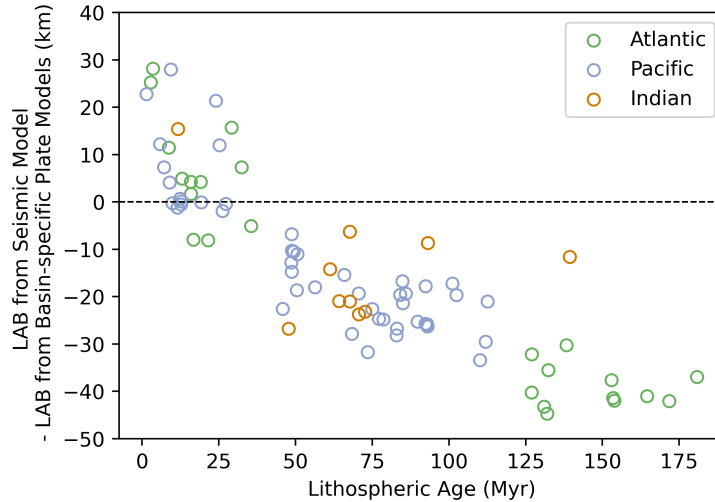


Figure 14. Difference between local lithospheric thickness beneath each island from the seismic model and that predicted by the basin-specific plate models, as a function of lithospheric age at time of OIB eruption. Localities in the Atlantic, Pacific and Indian Oceans are represented by green, blue and red circles, respectively.

795 lower than ~ 75 km and therefore smearing shallow velocity structure into greater depths
 796 in regions of thin lithosphere (see Section 2.2). For older lithosphere on the other hand,
 797 seismically inferred estimates of present-day lithospheric thickness beneath each ocean
 798 island are consistently thinner than expectations from plate models. In contrast to the
 799 artifacts in regions of thin lithosphere, this observation is likely real and probably reflects
 800 destabilisation and thinning of the lithosphere by the underlying mantle plume (e.g., G. F. Davies,
 801 1994; Dumoulin et al., 2001). As a consequence of these two effects, the majority of litho-
 802 spheric thickness estimates beneath OIBs from the seismic model fall in the 40–100 km
 803 range, which is slightly narrower than the associated range of 30–120 km from plate-cooling
 804 models.

805 When switching to estimates of lithospheric thickness inferred from the seismic model,
 806 we find that all geochemical trends are best fitted by bi-linear models, including those
 807 that display linear trends when using lithospheric thickness from basin-specific plate mod-
 808 els (Supplementary Figure S4f). In particular, there is a moderate preference ($5 < \log_{10} E_2 -$
 809 $\log_{10} E_1 < 10$) for bi-linear models in the cases of Al_2O_3 , FeO and Yb, as well as a slight
 810 preference ($2 < \log_{10} E_2 - \log_{10} E_1 < 5$) in the cases of SiO_2 , Lu, and λ_2 . Neverthe-
 811 less, constant models still perform poorly, and our dataset displays robust evidence for
 812 existence of the lid effect.

813 4.6 Processes Contributing to Observed Geochemical Trends

814 In our reference setup, bi-linear trends generally fall into two categories: (i) the highly
 815 incompatible elements (Th, K, La, P, Ti, Na), in which concentrations are entirely controlled
 816 by melt fraction and therefore indicate that F remains approximately constant
 817 at lithospheric thicknesses greater than that of the kink; and (ii) for CaO and param-
 818 eters describing REE patterns (λ_0 and λ_1), where the depth of the kink is being deter-
 819 mined by the combined effects of changing melt fraction interacting with the spinel-garnet
 820 phase transition. For the latter, the role of this phase change is to maintain HREE con-
 821 centrations with increasing lithospheric thickness, while allowing the concentration of
 822 the LREE to continue to increase as F reduces.

823 It is important to note that the kinks in our bi-linear trends may not, in reality,
 824 reflect sharp change points, but rather a gradual transition in the trend as a function
 825 of increasing lithospheric thickness. While our findings show that the kink is generally
 826 identified at a depth of 50–60 km (Supplementary Figure S3), since these trends are sensi-
 827 tive to both variations in F and the spinel-garnet phase transition, it is incorrect to
 828 infer the phase transition depth directly from the kink depth. This point is further em-
 829 phasised by the fact that we observe garnet signatures in some OIBs that are generated
 830 beneath thin lithosphere (e.g., through trends of Yb, Lu, λ_2), which can be attributed
 831 to the memory effect of high-pressure melts from the garnet stability field incompletely
 832 mixing with lower pressure melts from the spinel stability field.

833 Our resulting inferences of melt fraction as a function of lithospheric thickness (Fig-
 834 ure 12a) suggest that, beyond a certain lithospheric thickness, F becomes approximately
 835 constant. This behaviour is unexpected since, based on the lid effect and theoretical mod-
 836 els of plate cooling, we would expect lithosphere to continue to thicken and, all other as-
 837 pects being equal, cause a continuous reduction in F . One potential explanation for this
 838 behaviour could be progressive thinning of overlying lithosphere by upwelling plume mat-
 839 erial. Small-scale convection above mantle plumes is known to be more prevalent be-
 840 neath thicker lithosphere (e.g., Dumoulin et al., 2001; van Hunen et al., 2003; Ballmer
 841 et al., 2011; Le Voci et al., 2014; D. R. Davies et al., 2016; Duvernay et al., 2021), mak-
 842 ing it more likely that the base of older lithosphere would become unstable upon plume
 843 impingement. This argument is supported by our observation in Section 4.5.3 and Fig-
 844 ure 14 that seismically inferred estimates of lithospheric thickness are consistently thin-
 845 ner than those predicted by plate-cooling models in older lithosphere. Accordingly, be-
 846 yond the ~ 55 km kink depth, lithospheric thickness above mantle plumes is unlikely
 847 to increase at a rate consistent with cooling model expectations, thereby reducing the
 848 rate of the expected reduction in melt fraction. A further contributing factor is that, since
 849 the solidus temperature increases with pressure (Figure 12b), weaker plumes with lower
 850 excess temperatures may fail to cross the solidus and generate melt beneath thick litho-
 851 sphere. This effect would be compounded by the fact that weaker plumes generate smaller
 852 melt volumes that are more likely to get trapped at depth and not erupt onto the seafloor.
 853 We refer to this behaviour as the ‘temperature effect’ and have investigated two lines of
 854 independent evidence that might support it.

855 First, we have explored potential relationships between lithospheric thickness and
 856 the potential temperature of OIB sources as estimated from geochemical arguments (e.g.,
 857 Herzberg et al., 2007; Putirka, 2008). No clear patterns have emerged (although such
 858 estimates are known to be highly uncertain; e.g., Bao et al., 2022). Secondly, we have
 859 compared lithospheric thickness to recent analyses of plume buoyancy flux from Hoggard,
 860 Parnell-Turner, and White (2020). Here, we find that magmatic plumes beneath thicker
 861 lithosphere generally have higher buoyancy fluxes, potentially indicative of higher ex-
 862 cess temperatures (Figure 15). This observation is consistent with the suggestion that,
 863 beyond the kink depth, melt fractions are approximately constant due to preferential sam-
 864 pling of progressively hotter plumes from regions of thicker lithosphere (i.e., the rate of
 865 decrease in F is at least partially offset by the increase in plume temperature). An ad-
 866 ditional consideration is that plumes with higher buoyancy fluxes entrain greater vol-
 867 ume fractions of dense, primordial materials from their source regions (Jones et al., 2016;
 868 M. Jackson et al., 2017). Given that primordial materials generally have lower concen-
 869 trations of incompatible elements relative to mantle peridotites, this may imply that plumes
 870 erupting on thicker lithosphere contain lower concentrations of incompatible trace ele-
 871 ments to begin with.

872 Taken together, local variations in lithospheric thickness away from average expecta-
 873 tions from theoretical cooling models, sampling biases associated with progressively
 874 hotter plumes in regions of thicker lithosphere, and source region heterogeneities, are all
 875 plausible contributors to observed incompatible element trends.

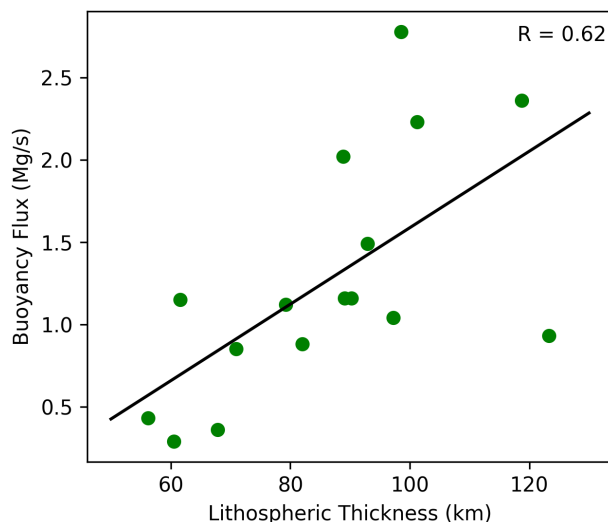


Figure 15. Relationship between buoyancy flux of magmatic plumes from Hoggard, Parnell-Turner, and White (2020) and lithospheric thickness estimated from the basin-specific plate models (for values greater than the kink depth of ~ 55 km).

876

4.7 Limited Evidence for Melt Re-equilibration at Base of Lithosphere

877

878

879

880

881

882

883

884

885

886

887

Both Iceland and Hawaii have a large number of samples and exhibit a wide spread of compositions (e.g. Figure 16). Previous studies have attributed these ranges to variations in fertility of the mantle source (e.g., Humphreys & Niu, 2009; Niu et al., 2011). Furthermore, Niu (2021) have also suggested that none of this spread can be attributed to differences in the initial melting pressure (i.e. there is no memory effect), since OIB melts re-equilibrate with surrounding mantle during their ascent to the surface. Melting in an ascending mantle plume is expected to occur over a depth range of several tens of kilometres. If such re-equilibration reactions do occur, however, we would expect major element concentrations buffered by olivine and pyroxene to be strongly homogenised, while highly incompatible trace elements (e.g., Th, K and La) that have $D' < 0.01$ in both the garnet and spinel stability fields should retain their original spread.

888

889

890

891

892

893

894

895

896

897

898

899

900

901

Our analyses have found no evidence to support such a process for re-equilibration of plume-derived melts: in other words, we find robust evidence for the memory effect. OIBs from Hawaii and Iceland, for example, show a negative correlation between SiO_2 and FeOT (Figure 16a–b), which can be attributed to melts generated at a range of different pressures and has previously been suggested to occur in many OIBs (e.g., Scarrow & Cox, 1995). In the case of Iceland, most of the data cluster at ~ 46.5 wt.% SiO_2 , but some samples extend towards ~ 42 wt.% SiO_2 . The high SiO_2 samples could relate to melts generated at low pressure, while samples with lower SiO_2 are generated by smaller degrees of melting at higher pressure. There is also a cluster of samples at the high SiO_2 end of the Hawaiian array, albeit at 48.5 wt.% SiO_2 , with the data more evenly spread across the array. As with Iceland, we suggest that the low- SiO_2 , high-FeOT basalts at Hawaii are produced by melts separating from the mantle at depth (i.e. far below the lithospheric lid) and that they have subsequently erupted without undergoing re-equilibration during their ascent.

902

903

904

Importantly, whilst variations in FeOT at a given SiO_2 can potentially be explained by mantle source heterogeneity, the correlation between SiO_2 and λ_1 provides convincing support for melting across a range of pressures with minimal re-equilibration (Fig-

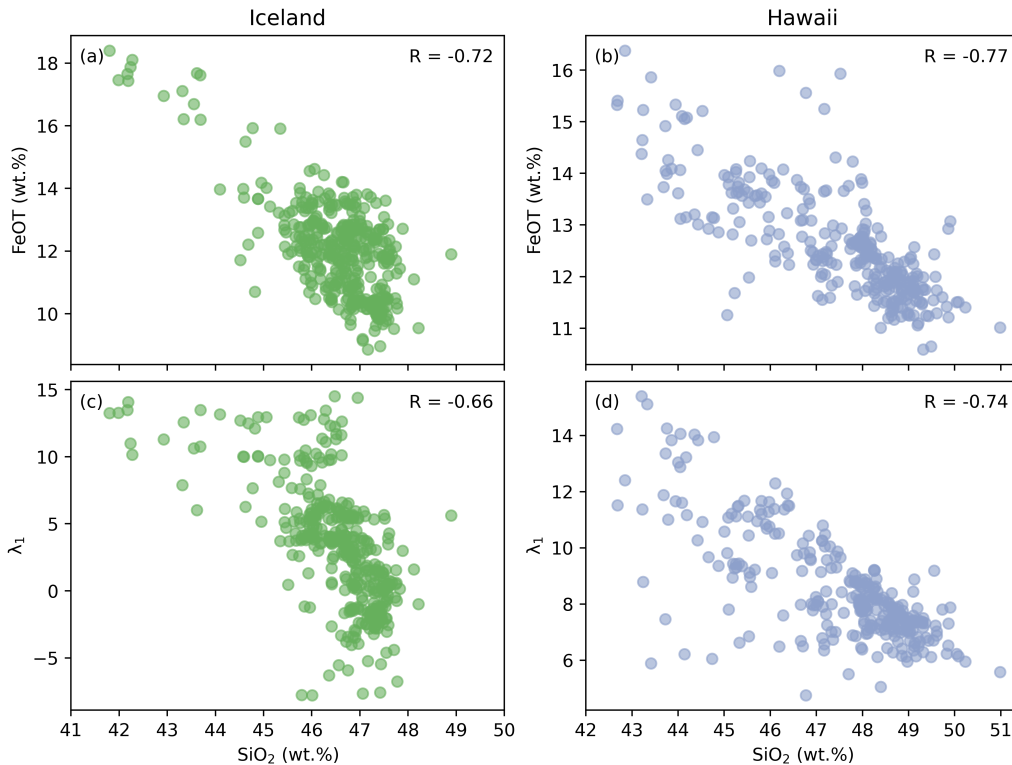


Figure 16. Co-variation of pressure-sensitive geochemical parameters for OIB samples located at Iceland and Hawaii. (a) FeOT as a function of SiO₂ for Icelandic samples, following application of filtering and corrections for fractional crystallisation. (b) Same for Hawaiian samples. (c-d) Same for λ₁ values as a function of SiO₂.

905 ure 16c-d). Melt re-equilibration would be expected to bound major element concentrations within a limited range, but have next-to-no impact on incompatible trace element concentrations. Accordingly, following re-equilibration, no correlation would be expected between major and trace elements, which is not borne out by our observations.

909 5 Conclusions

910 Our study yields insights into the role of lithospheric thickness variations in influencing the geochemical characteristics of OIBs. We confirm existence of the lid effect, 911 in that lithospheric thickness limits the lowest melting pressure of upwelling mantle plumes. 912 Our statistical analyses demonstrate that REE patterns, major and trace element concentrations are all influenced by lithospheric thickness, with some geochemical parameters best fitted by linear trends and others by bi-linear trends with a kink at thicknesses 913 of 50–60 km. Although these trends can be sensitive to source composition, potential bias from heavily sampled localities, and choice of lithospheric thickness estimate, overall patterns are consistent, and our explanations for their behaviour appear robust. 914 915 916 917 918

919 Such trends can be explained by pressure-driven changes in mineral assemblage and melt fraction, or through effects associated with the spinel-garnet transition. Notably, 920 the behavior of highly incompatible elements in localities on thin lithosphere suggests that melt fraction decreases rapidly with increasing lithospheric thickness until thicknesses of ~ 55 km, but subsequently decreases at a significantly lower rate at greater thick- 921 922 923

nesses. This behaviour is inconsistent with theoretical expectations and suggests that: (i) plumes impinging beneath thicker lithosphere may be more effective at thinning the overlying lid, thereby modulating changes in melt fraction; and (ii) only melts from plumes with higher potential temperatures are able to penetrate thick lithosphere and reach the seafloor, consistent with solidus temperatures increasing with pressure and evidence that magmatic plumes under thicker lithosphere have higher buoyancy fluxes.

The exact depth of the spinel-garnet transition zone cannot be identified from the trends considered herein. Nonetheless, the signature of this phase transition is evident in observed trends for Yb, Lu, and λ_2 . In addition, these trends require that a signature of melting within the garnet stability field is carried by some OIBs originating beneath thin lithosphere, indicative of a memory effect within plume-derived melts. This interpretation is further supported by geochemical trends from different samples generated in the same plume: it is plausible that some OIB melts generated at varying pressures can ascend to the surface without re-equilibrating at the base of the lithosphere.

Open Research

The OIB geochemistry, lithospheric thickness, and other data files are achieved at <https://zenodo.org/records/10464062>. The Python scripts for Bayes factor analysis are available at <https://github.com/shihao-jiang/BayesFactors>. Figures have been prepared using Matplotlib (Hunter, 2007).

Acknowledgments

This research was undertaken with the assistance of resources from the *National Computational Infrastructure* (NCI Australia), an NCRIS enabled capability supported by the Australian Government, and was partially supported by the Australian Government through the *Australian Research Council's* Discovery Projects funding scheme (project DP200100053) and Discovery Early Career Researcher Awards (DE220101519). The authors are also grateful for funding provided by the *Chinese Scholarship Council* (CSC) scholarship and *Shen-su Sun* scholarship. We thank Anthony Burnham, Thomas Duvernay, Hugh O'Neill and Fred Richards for help and feedback.

References

- Ahrens, L. H. (1952). The use of ionization potentials Part 1. Ionic radii of the elements. *Geochim. Cosmochim. Acta*, *2*(3), 155–169.
- Albarède, F., Luais, B., Fitton, G., Semet, M., Kaminski, E., Upton, B. G. J., . . . Cheminée, J.-L. (1997). The geochemical regimes of Piton de la Fournaise volcano (Réunion) during the last 530000 years. *J. Petrol.*, *38*(2), 171–201.
- Asimow, P. D., & Langmuir, C. (2003). The importance of water to oceanic mantle melting regimes. *Nature*, *421*(6925), 815–820.
- Ball, P. W., Duvernay, T., & Davies, D. R. (2022). A coupled geochemical-geodynamic approach for predicting mantle melting in space and time. *Geochem. Geophys. Geosys.*, *23*(4), e2022GC010421.
- Ball, P. W., White, N. J., Masoud, A., Nixon, S., Hoggard, M. J., MacLennan, J., . . . Kröpelin, S. (2019). Quantifying asthenospheric and lithospheric controls on mafic magmatism across North Africa. *Geochem. Geophys. Geosys.*, *20*(7), 3520–3555.
- Ballmer, M. D., Ito, G., van Hunen, J., & Tackley, P. J. (2011). Spatial and temporal variability in Hawaiian hotspot volcanism induced by small-scale convection. *Nat. Geosci.*, *4*(7), 457–460.
- Bao, X., Lithgow-Bertelloni, C. R., Jackson, M. G., & Romanowicz, B. (2022). On the relative temperatures of Earth's volcanic hotspots and mid-ocean ridges.

- 972 *Science*, 375(6576), 57–61.
- 973 Bohlen, S. R., & Boettcher, A. L. (1981). Experimental investigations and geological
974 applications of orthopyroxene geobarometry. *Am. Mineral.*, 66(9-10), 951–964.
- 975 Bohlen, S. R., Essene, E. J., & Boettcher, A. L. (1980). Reinvestigation and applica-
976 tion of olivine-quartz-orthopyroxene barometry. *Earth Planet. Sci. Lett.*, 47(1),
977 1–10.
- 978 Borghini, G., Fumagalli, P., & Rampone, E. (2010). The stability of plagioclase in
979 the upper mantle: subsolidus experiments on fertile and depleted lherzolite. *J.*
980 *Petrol.*, 51(1-2), 229–254.
- 981 Burov, E., & Gerya, T. (2014). Asymmetric three-dimensional topography over man-
982 tle plumes. *Nature*, 513(7516), 85–89.
- 983 Burov, E., Guillou-Frottier, L., d’Acremont, E., Le Pourhiet, L., & Cloetingh, S.
984 (2007). Plume head–lithosphere interactions near intra-continental plate
985 boundaries. *Tectonophysics*, 434(1-4), 15–38.
- 986 Campbell, I. H. (2007). Testing the plume theory. *Chem. Geol.*, 241(3-4), 153–176.
- 987 Campbell, I. H., & Borley, G. D. (1974). The geochemistry of pyroxenes from the
988 lower layered series of the Jimberlana intrusion, Western Australia. *Contrib.*
989 *Mineral. Petrol.*, 47(4), 281–297.
- 990 Campbell, I. H., & Nolan, J. (1974). Factors effecting the stability field of Ca-poor
991 pyroxene and the origin of the Ca-poor minimum in Ca-rich pyroxenes from
992 tholeiitic intrusions. *Contrib. Mineral. and Petrol.*, 48(3), 205–219.
- 993 Chung, S.-L., & Jahn, B.-M. (1995). Plume-lithosphere interaction in generation of
994 the Emeishan flood basalts at the Permian-Triassic boundary. *Geology*, 23(10),
995 889–892.
- 996 Class, C., & Goldstein, S. L. (1997). Plume-lithosphere interactions in the ocean
997 basins: constraints from the source mineralogy. *Earth Planet. Sci. Lett.*, 150(3-
998 4), 245–260.
- 999 Colson, R. O., & Gust, D. A. (1989). Effects of pressure on partitioning of trace ele-
1000 ments between low-Ca pyroxene and melt. *Am. Mineral.*, 74(1-2), 31–36.
- 1001 Condie, K. C. (1999). Mafic crustal xenoliths and the origin of the lower continental
1002 crust. *Lithos*, 46(1), 95–101.
- 1003 Courtillot, V., Jaupart, C., Manighetti, I., Tapponnier, P., & Besse, J. (1999). On
1004 causal links between flood basalts and continental breakup. *Earth Planet. Sci.*
1005 *Lett.*, 166(3-4), 177–195.
- 1006 Danyushevsky, L. V., & Plechov, P. (2011). Petrolog3: Integrated software for mod-
1007 eling crystallization processes. *Geochem. Geophys. Geosys.*, 12(7).
- 1008 Dasgupta, R., Jackson, M. G., & Lee, C.-T. A. (2010). Major element chemistry of
1009 ocean island basalts—conditions of mantle melting and heterogeneity of mantle
1010 source. *Earth Planet. Sci. Lett.*, 289(3-4), 377–392.
- 1011 Davies, D. R., & Davies, J. H. (2009). Thermally-driven mantle plumes reconcile
1012 multiple hot-spot observations. *Earth Planet. Sci. Lett.*, 278(1-2), 50–54.
- 1013 Davies, D. R., Goes, S., & Sambridge, M. (2015). On the relationship between
1014 volcanic hotspot locations, the reconstructed eruption sites of large igneous
1015 provinces and deep mantle seismic structure. *Earth Planet. Sci. Lett.*, 411,
1016 121–130.
- 1017 Davies, D. R., Le Voci, G., Goes, S., Kramer, S. C., & Wilson, C. R. (2016). The
1018 mantle wedge’s transient 3-D flow regime and thermal structure. *Geochem.*
1019 *Geophys. Geosys.*, 17(1), 78–100.
- 1020 Davies, D. R., Rawlinson, N., Iaffaldano, G., & Campbell, I. H. (2015). Lithospheric
1021 controls on magma composition along Earth’s longest continental hotspot
1022 track. *Nature*, 525(7570), 511–514.
- 1023 Davies, D. R., Valentine, A., Kramer, S. C., Rawlinson, N., Hoggard, M. J., Eakin,
1024 C., & Wilson, C. (2019). Earth’s multi-scale topographic response to global
1025 mantle flow. *Nat. Geosci.*, 12(10), 845–850.

- 1026 Davies, G. F. (1994). Thermomechanical erosion of the lithosphere by mantle
1027 plumes. *J. Geophys. Res.*, *99*(B8), 15709–15722.
- 1028 Davies, J. H. F. L., Marzoli, A., Bertrand, H., Youbi, N., Ernesto, M., Greber, N.,
1029 ... others (2021). Zircon petrochronology in large igneous provinces reveals
1030 upper crustal contamination processes: new U–Pb ages, Hf and O isotopes,
1031 and trace elements from the Central Atlantic magmatic province (CAMP).
1032 *Contrib. Mineral. Petrol.*, *176*, 1–24.
- 1033 Dumoulin, C., Doin, M.-P., & Fleitout, L. (2001). Numerical simulations of the cool-
1034 ing of an oceanic lithosphere above a convective mantle. *Phys. Earth Planet.*
1035 *Inter.*, *125*(1-4), 45–64.
- 1036 Duncan, R. A., & Richards, M. (1991). Hotspots, mantle plumes, flood basalts, and
1037 true polar wander. *Rev. Geophys.*, *29*(1), 31–50.
- 1038 Duvernay, T., Davies, D. R., Mathews, C. R., Gibson, A. H., & Kramer, S. C.
1039 (2021). Linking intraplate volcanism to lithospheric structure and astheno-
1040 spheric flow. *Geochem. Geophys. Geosys.*, *22*(8), e2021GC009953.
- 1041 Duvernay, T., Davies, D. R., Mathews, C. R., Gibson, A. H., & Kramer, S. C.
1042 (2022). Continental magmatism: the surface manifestation of dynamic interac-
1043 tions between cratonic lithosphere, mantle plumes and edge-driven convection.
1044 *Geochem. Geophys. Geosys.*, *23*(7), e2022GC010363.
- 1045 Ellam, R. (1992). Lithospheric thickness as a control on basalt geochemistry. *Geol-*
1046 *ogy*, *20*(2), 153–156.
- 1047 Elliott, T., Hawkesworth, C., & Grönvold, K. (1991). Dynamic melting of the Ice-
1048 land plume. *Nature*, *351*(6323), 201–206.
- 1049 Fisk, M., Upton, B., Ford, C., & White, W. (1988). Geochemical and experimental
1050 study of the genesis of magmas of Reunion Island, Indian Ocean. *J. Geophys.*
1051 *Res.*, *93*(B5), 4933–4950.
- 1052 Fitton, J. G., James, D., & Leeman, W. P. (1991). Basic magmatism associated with
1053 late Cenozoic extension in the western United States: Compositional variations
1054 in space and time. *J. Geophys. Res.*, *96*(B8), 13693–13711.
- 1055 Fujimaki, H., Tatsumoto, M., & Ken-ichiro, A. (1984). Partition coefficients of
1056 Hf, Zr, and REE between phenocrysts and groundmasses. *J. Geophys. Res.*,
1057 *89*(S02), 662–672.
- 1058 Gautier, I., Weis, D., Mennessier, J.-P., Vidal, P., Giret, A., & Loubet, M. (1990).
1059 Petrology and geochemistry of the Kerguelen Archipelago basalts (South In-
1060 dian Ocean): evolution of the mantle sources from ridge to intraplate position.
1061 *Earth Planet. Sci. Lett.*, *100*(1-3), 59–76.
- 1062 Gibson, S., & Geist, D. (2010). Geochemical and geophysical estimates of litho-
1063 spheric thickness variation beneath galápagos. *Earth Planet. Sci. Lett.*, *300*(3-
1064 4), 275–286.
- 1065 Goslin, J., & Sibuet, J.-C. (1975). Geophysical study of the easternmost Walvis
1066 Ridge, South Atlantic: deep structure. *Geol. Soc. Am. Bull.*, *86*(12), 1713–
1067 1724.
- 1068 Graça, M. C., Kuszniir, N., & Stanton, N. S. G. (2019). Crustal thickness mapping of
1069 the central South Atlantic and the geodynamic development of the Rio Grande
1070 Rise and Walvis Ridge. *Mar. Pet. Geol.*, *101*, 230–242.
- 1071 Green, D., & Ringwood, A. (1967). The genesis of basaltic magmas. *Contrib. Min-*
1072 *eral. Petrol.*, *15*(2), 103–190.
- 1073 Greenberger, R., Mustard, J., Kumar, P., Dyar, M., Breves, E., & Sklute, E. (2012).
1074 Low temperature aqueous alteration of basalt: Mineral assemblages of Deccan
1075 basalts and implications for Mars. *J. Geophys. Res.*, *117*(E11).
- 1076 Grevemeyer, I., Flueh, E. R., Reichert, C., Bialas, J., Kläschen, D., & Kopp, C.
1077 (2001). Crustal architecture and deep structure of the Ninetyeast Ridge
1078 hotspot trail from active-source ocean bottom seismology. *Geophys. J. Int.*,
1079 *144*(2), 414–431.
- 1080 Griffiths, R. W., & Campbell, I. H. (1990). Stirring and structure in mantle starting

- 1081 plumes. *Earth Planet. Sci. Lett.*, *99*(1-2), 66–78.
- 1082 Griffiths, R. W., & Campbell, I. H. (1991). On the dynamics of long-lived plume
1083 conduits in the convecting mantle. *Earth Planet. Sci. Lett.*, *103*(1-4), 214–227.
- 1084 Hart, S., Hauri, E., Oschmann, L., & Whitehead, J. (1992). Mantle plumes and en-
1085 trainment: isotopic evidence. *Science*, *256*(5056), 517–520.
- 1086 Herzberg, C. (1992). Depth and degree of melting of komatiites. *J. Geophys. Res.*,
1087 *97*(B4), 4521–4540.
- 1088 Herzberg, C., Asimow, P. D., Arndt, N., Niu, Y., Leshner, C., Fitton, J., ... Saun-
1089 ders, A. (2007). Temperatures in ambient mantle and plumes: Constraints
1090 from basalts, picrites, and komatiites. *Geochem. Geophys. Geosys.*, *8*(2).
- 1091 Hill, R. I. (1991). Starting plumes and continental break-up. *Earth Planet. Sci.*
1092 *Lett.*, *104*(2-4), 398–416.
- 1093 Hofmann, A. (2003). Sampling mantle heterogeneity through oceanic basalts: iso-
1094 topes and trace elements. *Treatise Geochem.*, *2*, 568.
- 1095 Hofmann, A., & Jochum, K. (1996). Source characteristics derived from very incom-
1096 compatible trace elements in Mauna Loa and Mauna Kea basalts, Hawaii Scientific
1097 Drilling Project. *J. Geophys. Res.*, *101*(B5), 11831–11839.
- 1098 Hoggard, M. J., Czarnota, K., Richards, F. D., Huston, D. L., Jaques, A. L., & Ghe-
1099 lichkhan, S. (2020). Global distribution of sediment-hosted metals controlled
1100 by craton edge stability. *Nat. Geosci.*, *13*(7), 504–510.
- 1101 Hoggard, M. J., Parnell-Turner, R., & White, N. (2020). Hotspots and mantle
1102 plumes revisited: Towards reconciling the mantle heat transfer discrepancy.
1103 *Earth Planet. Sci. Lett.*, *542*, 116317.
- 1104 Hole, M. J., & Millett, J. (2016). Controls of mantle potential temperature and
1105 lithospheric thickness on magmatism in the North Atlantic Igneous Province.
1106 *J. Petrol.*, *57*(2), 417–436.
- 1107 Humphreys, E. R., & Niu, Y. (2009). On the composition of ocean island basalts
1108 (OIB): The effects of lithospheric thickness variation and mantle metasoma-
1109 tism. *Lithos*, *112*(1-2), 118–136.
- 1110 Hunter, J. D. (2007). Matplotlib: A 2D graphics environment. *Computing in Science*
1111 *& Engineering*, *9*(3), 90–95. doi: 10.1109/MCSE.2007.55
- 1112 Iaffaldano, G., Davies, D. R., & DeMets, C. (2018). Indian Ocean floor deformation
1113 induced by the Reunion plume rather than the Tibetan Plateau. *Nat. Geosci.*,
1114 *11*(5), 362–366.
- 1115 Jackson, M., Konter, J., & Becker, T. (2017). Primordial helium entrained by the
1116 hottest mantle plumes. *Nature*, *542*(7641), 340–343.
- 1117 Jackson, M. G., Weis, D., & Huang, S. (2012). Major element variations in Hawaiian
1118 shield lavas: Source features and perspectives from global ocean island basalt
1119 (OIB) systematics. *Geochem. Geophys. Geosys.*, *13*(9).
- 1120 Jeffreys, H. (1935). Some tests of significance, treated by the theory of probability.
1121 In *Mathematical proceedings of the cambridge philosophical society* (Vol. 31, pp.
1122 203–222).
- 1123 Johnson, K. T. M. (1994). Experimental cpx/ and garnet/melt partitioning of REE
1124 and other trace elements at high pressures: petrogenetic implications. *Mineral*
1125 *Mag.*, *58A*(1), 454–455.
- 1126 Johnson, K. T. M. (1998). Experimental determination of partition coefficients for
1127 rare earth and high-field-strength elements between clinopyroxene, garnet, and
1128 basaltic melt at high pressures. *Contrib. Mineral. Petrol.*, *133*(1-2), 60–68. doi:
1129 DOI10.1007/s004100050437
- 1130 Jones, T. D., Davies, D. R., Campbell, I. H., Iaffaldano, G., Yaxley, G. M., Kramer,
1131 S. C., & Wilson, C. R. (2017). The concurrent emergence and causes of double
1132 volcanic hotspot tracks on the Pacific plate. *Nature*, *545*(7655), 472–476.
- 1133 Jones, T. D., Davies, D. R., Campbell, I. H., Wilson, C. R., & Kramer, S. C. (2016).
1134 Do mantle plumes preserve the heterogeneous structure of their deep-mantle
1135 source? *Earth Planet. Sci. Lett.*, *434*, 10–17.

- 1136 Jones, T. D., Davies, D. R., & Sossi, P. A. (2019). Tungsten isotopes in mantle
1137 plumes: Heads it's positive, tails it's negative. *Earth Planet. Sci. Lett.*, *506*,
1138 255–267.
- 1139 Kass, R. E., & Raftery, A. E. (1995). Bayes factors. *J. Am. Stat. Assoc.*, *90*(430),
1140 773–795.
- 1141 Katz, R. F., Spiegelman, M., & Langmuir, C. H. (2003). A new parameterization of
1142 hydrous mantle melting. *Geochem., Geophys., Geosys.*, *4*(9).
- 1143 Khogenkumar, S., Singh, A. K., Singh, R. B., Khanna, P., Singh, N. I., & Singh,
1144 W. I. (2016). Coexistence of MORB and OIB-type mafic volcanics in the
1145 Manipur Ophiolite Complex, Indo-Myanmar Orogenic Belt, northeast India:
1146 implication for heterogeneous mantle source at the spreading zone. *J. Asian
1147 Earth Sci.*, *116*, 42–58.
- 1148 Klemme, S., & O'Neill, H. S. (2000). The near-solidus transition from garnet lherzo-
1149 lite to spinel lherzolite. *Contrib. Mineral. Petrol.*, *138*(3), 237–248.
- 1150 Klöcking, M., White, N., MacLennan, J., McKenzie, D., & Fitton, J. (2018). Quan-
1151 titative relationships between basalt geochemistry, shear wave velocity, and
1152 asthenospheric temperature beneath western North America. *Geochem. Geo-
1153ophys. Geosys.*, *19*(9), 3376–3404.
- 1154 Le Voci, G., Davies, D. R., Goes, S., Kramer, S. C., & Wilson, C. R. (2014). A
1155 systematic 2-D investigation into the mantle wedge's transient flow regime and
1156 thermal structure: Complexities arising from a hydrated rheology and thermal
1157 buoyancy. *Geochem. Geophys. Geosys.*, *15*(1), 28–51.
- 1158 Li, M., McNamara, A. K., & Garnero, E. J. (2014). Chemical complexity of hotspots
1159 caused by cycling oceanic crust through mantle reservoirs. *Nat. Geosci.*, *7*(5),
1160 366–370.
- 1161 Liu, J.-Q., Chen, L.-H., Zeng, G., Wang, X.-J., Zhong, Y., & Yu, X. (2016). Litho-
1162 spheric thickness controlled compositional variations in potassic basalts of
1163 Northeast China by melt-rock interactions. *Geophys. Res. Lett.*, *43*(6), 2582–
1164 2589.
- 1165 Lundstrom, C. C., Hoernle, K., & Gill, J. (2003). U-series disequilibria in volcanic
1166 rocks from the Canary Islands: Plume versus lithospheric melting. *Geochim.
1167 Cosmochim. Acta*, *67*(21), 4153–4177.
- 1168 MacDonald, G. A., & Katsura, T. (1964). Chemical composition of Hawaiian lavas.
1169 *J. Petrol.*, *5*(1), 82–133.
- 1170 Masaaki, O. (1980). The Ronda peridotite: Garnet-, spinel-, and plagioclase-
1171 lherzolite facies and the PT trajectories of a high-temperature mantle intrusion.
1172 *J. Petrol.*, *21*(3), 533–572.
- 1173 McKenzie, D. (1967). Some remarks on heat flow and gravity anomalies. *J. Geophys.
1174 Res.*, *72*(24), 6261–6273.
- 1175 McKenzie, D., & O'Nions, R. K. (1991). Partial melt distributions from inversion of
1176 rare earth element concentrations. *J. Petrol.*, *32*(5), 1021–1091.
- 1177 Morgan, W. J. (1971). Convection plumes in the lower mantle. *Nature*, *230*(5288),
1178 42–43.
- 1179 Nebel, O., Sossi, P. A., Bénard, A., Arculus, R. J., Yaxley, G. M., Woodhead, J. D.,
1180 ... Ruttor, S. (2019). Reconciling petrological and isotopic mixing mechanisms
1181 in the Pitcairn mantle plume using stable Fe isotopes. *Earth Planet. Sci. Lett.*,
1182 *521*, 60–67.
- 1183 Niu, Y. (2016). The meaning of global ocean ridge basalt major element composi-
1184 tions. *J. Petrol.*, *57*(11-12), 2081–2103.
- 1185 Niu, Y. (2021). Lithosphere thickness controls the extent of mantle melting, depth
1186 of melt extraction and basalt compositions in all tectonic settings on Earth –
1187 A review and new perspectives. *Earth-Science Reviews*, *217*, 103614.
- 1188 Niu, Y., Wilson, M., Humphreys, E. R., & O'Hara, M. J. (2011). The origin of
1189 intra-plate ocean island basalts (OIB): the lid effect and its geodynamic impli-
1190 cations. *J. Petrol.*, *52*(7-8), 1443–1468.

- 1191 Norman, M. D., & Garcia, M. O. (1999). Primitive magmas and source character-
 1192 istics of the Hawaiian plume: petrology and geochemistry of shield picrites.
 1193 *Earth Planet. Sci. Lett.*, *168*(1-2), 27–44.
- 1194 Owen-Smith, T. M., Ashwal, L. D., Sudo, M., & Trumbull, R. B. (2017). Age
 1195 and petrogenesis of the Doros Complex, Namibia, and implications for early
 1196 plume-derived melts in the Paraná–Etendeka LIP. *J. Petrol.*, *58*(3), 423–442.
- 1197 O’Neill, H. S. C. (2016). The smoothness and shapes of chondrite-normalized rare
 1198 earth element patterns in basalts. *J. Petrol.*, *57*(8), 1463–1508.
- 1199 Pallister, J. S., & Hopson, C. A. (1981). Samail ophiolite plutonic suite: field
 1200 relations, phase variation, cryptic variation and layering, and a model of a
 1201 spreading ridge magma chamber. *J. Geophys. Res.*, *86*(B4), 2593–2644.
- 1202 Parsons, B., & Sclater, J. G. (1977). An analysis of the variation of ocean floor
 1203 bathymetry and heat flow with age. *J. Geophys. Res.*, *82*(5), 803–827.
- 1204 Pietruszka, A. J., Norman, M. D., Garcia, M. O., Marske, J. P., & Burns, D. H.
 1205 (2013). Chemical heterogeneity in the hawaiian mantle plume from the alter-
 1206 ation and dehydration of recycled oceanic crust. *Earth Planet. Sci. Lett.*, *361*,
 1207 298–309.
- 1208 Priestley, K., & McKenzie, D. (2006). The thermal structure of the lithosphere from
 1209 shear wave velocities. *Earth Planet. Sci. Lett.*, *244*(1-2), 285–301.
- 1210 Putirka, K. (2008). Excess temperatures at ocean islands: Implications for mantle
 1211 layering and convection. *Geology*, *36*(4), 283–286.
- 1212 Richards, F. D., Hoggard, M. J., Cowton, L. R., & White, N. J. (2018). Reassessing
 1213 the thermal structure of oceanic lithosphere with revised global inventories
 1214 of basement depths and heat flow measurements. *J. Geophys. Res.*, *123*(10),
 1215 9136–9161.
- 1216 Richards, F. D., Hoggard, M. J., Crosby, A., Ghelichkhan, S., & White, N. (2020).
 1217 Structure and dynamics of the oceanic lithosphere-asthenosphere system. *Phys.*
 1218 *Earth Planet. Inter.*, *309*, 106559.
- 1219 Richards, F. D., Hoggard, M. J., White, N., & Ghelichkhan, S. (2020). Quantifying
 1220 the relationship between short-wavelength dynamic topography and thermo-
 1221 mechanical structure of the upper mantle using calibrated parameterization of
 1222 anelasticity. *J. Geophys. Res.*, *125*(9), e2019JB019062.
- 1223 Robinson, J. A. C., & Wood, B. J. (1998). The depth of the spinel to garnet transi-
 1224 tion at the peridotite solidus. *Earth Planet. Sci. Lett.*, *164*(1-2), 277–284.
- 1225 Rudnick, R. L. (1995). Making continental crust. *Nature*, *378*(6557), 571–578.
- 1226 Ryan, M. P. (1988). The mechanics and three-dimensional internal structure of
 1227 active magmatic systems: Kilauea Volcano, Hawaii. *J. Geophys. Res.*, *93*(B5),
 1228 4213–4248.
- 1229 Ryan, M. P. (1994). Neutral-buoyancy controlled magma transport and storage in
 1230 mid-ocean ridge magma reservoirs and their sheeted-dike complex: a summary
 1231 of basic relationships. *Int. Geophys.*, *57*, 97–138.
- 1232 Safonov, O., Bindi, L., & Vinograd, V. (2011). Potassium-bearing clinopyroxene: a
 1233 review of experimental, crystal chemical and thermodynamic data with petro-
 1234 logical applications. *Mineral. Mag.*, *75*(4), 2467–2484.
- 1235 Saito, T., Uno, M., Sato, T., Fujisaki, W., Haraguchi, S., Li, Y.-b., . . . Maruyama,
 1236 S. (2015). Geochemistry of accreted metavolcanic rocks from the Neoprotero-
 1237 zoic Gwna Group of Anglesey–Lleyn, NW Wales, UK: MORB and OIB in the
 1238 Iapetus Ocean. *Tectonophysics*, *662*, 243–255.
- 1239 Scarrow, J. H., & Cox, K. (1995). Basalts generated by decompressive adiabatic
 1240 melting of a mantle plume: a case study from the Isle of Skye, NW Scotland.
 1241 *J. Petrol.*, *36*(1), 3–22.
- 1242 Schaeffer, A., & Lebedev, S. (2013). Global shear speed structure of the upper man-
 1243 tle and transition zone. *Geophys. J. Int.*, *194*(1), 417–449.
- 1244 Schmincke, H.-U. (1982). Volcanic and chemical evolution of the Canary Islands. In
 1245 *Geology of the northwest african continental margin* (pp. 273–306). Springer.

- 1246 Seton, M., Müller, R. D., Zahirovic, S., Williams, S., Wright, N. M., Cannon, J.,
 1247 ... McGirr, R. (2020). A global data set of present-day oceanic crustal age
 1248 and seafloor spreading parameters. *Geochem. Geophys. Geosys.*, *21*(10),
 1249 e2020GC009214.
- 1250 Shaw, D. M. (1970). Trace element fractionation during anatexis. *Geochim. Cos-*
 1251 *mochim. Acta*, *34*(2), 237–243.
- 1252 Shaw, D. M. (1979). Trace element melting models. *Phys. Chem. Earth*, *11*, 577–
 1253 586.
- 1254 Sisson, T., & Grove, T. (1993). Temperatures and H₂O contents of low-MgO high-
 1255 alumina basalts. *Contrib. Mineral. Petrol.*, *113*(2), 167–184.
- 1256 Skilling, J. (2006). Nested sampling for general bayesian computation. *Bayesian*
 1257 *Anal.*, *1*(4), 833–860.
- 1258 Speagle, J. S. (2020). DYNESTY: a dynamic nested sampling package for estimating
 1259 Bayesian posteriors and evidences. *Mon. Notices Royal Astron. Soc.*, *493*(3),
 1260 3132–3158.
- 1261 Straub, S. M., Gómez-Tuena, A., Zellmer, G. F., Espinasa-Perena, R., Stuart, F. M.,
 1262 Cai, Y., ... Mesko, G. T. (2013). The processes of melt differentiation in arc
 1263 volcanic rocks: Insights from OIB-type arc magmas in the central Mexican
 1264 volcanic belt. *J. Petrol.*, *54*(4), 665–701.
- 1265 Sun, C., & Liang, Y. (2013). The importance of crystal chemistry on REE parti-
 1266 tioning between mantle minerals (garnet, clinopyroxene, orthopyroxene, and
 1267 olivine) and basaltic melts. *Chem. Geol.*, *358*, 23–36.
- 1268 Tomlinson, E. L., & Holland, T. J. (2021). A thermodynamic model for the sub-
 1269 solidus evolution and melting of peridotite. *J. Petrol.*, *62*(1), 1–23.
- 1270 Turcotte, D. L., & Oxburgh, E. R. (1967). Finite amplitude convective cells
 1271 and continental drift. *J. Fluid Mech.*, *28*(1), 29–42. doi: 10.1017/
 1272 S0022112067001880
- 1273 Ubide, T., Larrea, P., Becerril, L., & Galé, C. (2022). Volcanic plumbing filters on
 1274 ocean-island basalt geochemistry. *Geology*, *50*(1), 26–31.
- 1275 van Hunen, J., Huang, J., & Zhong, S. (2003). The effect of shearing on the on-
 1276 set and vigor of small-scale convection in a Newtonian rheology. *Geophys. Res.*
 1277 *Lett.*, *30*(19).
- 1278 Wallace, P. J. (1998). Water and partial melting in mantle plumes: Inferences from
 1279 the dissolved H₂O concentrations of Hawaiian basaltic magmas. *Geophys. Res.*
 1280 *Lett.*, *25*(19), 3639–3642.
- 1281 Walter, M. J., & Presnall, D. C. (1994). Melting behavior of simplified lherzolite in
 1282 the system CaO-MgO-Al₂O₃-SiO₂-Na₂O from 7 to 35 kbar. *J. Petrol.*, *35*(2),
 1283 329–359.
- 1284 Watson, S., & McKenzie, D. (1991). Melt generation by plumes: a study of Hawai-
 1285 ian volcanism. *J. Petrol.*, *32*(3), 501–537.
- 1286 Weaver, B. L. (1991). The origin of ocean island basalt end-member compositions:
 1287 trace element and isotopic constraints. *Earth Planet. Sci. Lett.*, *104*(2-4), 381–
 1288 397.
- 1289 White, R., & McKenzie, D. (1989). Magmatism at rift zones: the generation of vol-
 1290 canic continental margins and flood basalts. *J. Geophys. Res.*, *94*(B6), 7685–
 1291 7729.
- 1292 White, R., Minshull, T., Richardson, K., Smallwood, J., Staples, R., McBride, J., ...
 1293 Group, F. W. (1996). Seismic images of crust beneath Iceland contribute to
 1294 long-standing debate. *Eos, Transactions American Geophysical Union*, *77*(21),
 1295 197–201.
- 1296 Wood, B. J., Kiseeva, E. S., & Matzen, A. K. (2013). Garnet in the Earth’s Mantle.
 1297 *Elements*, *9*(6), 421–426.
- 1298 Yoder Jr, H., & Tilley, C. E. (1962). Origin of basalt magmas: an experimental
 1299 study of natural and synthetic rock systems. *J. Petrol.*, *3*(3), 342–532.